Design of highly microporous activated carbons based on walnut shell biomass for H2 and CO2 storage

Carbon 201 (2023) 633–647

Contents lists available at ScienceDirect

Carbon

journal homepage: www.elsevier.com/locate/carbon

Design of highly microporous activated carbons based on walnut shell biomass for H_2 and CO_2 storage

Jarosław Serafin [a,*], Bartosz Dziejarski [b,c], Orlando F. Cruz Junior [d], Joanna Sreńscek-Nazzal [e]

[a] Department of Inorganic and Organic Chemistry, University of Barcelona, Martí i Franquès, 1-11, 08028, Barcelona, Spain
[b] Faculty of Environmental Engineering, Wroclaw University of Science and Technology, 50-370, Wroclaw, Poland
[c] Department of Space, Earth and Environment, Chalmers University of Technology, SE-412 96, Göteborg, Sweden
[d] Laboratory of Microscopy and Nanotechnology, National Institute of Amazonian Research, Av. André Araújo, 2936, Petrópolis, Manaus, AM, 69067-375, Brazil
[e] West Pomeranian University of Technology in Szczecin, Faculty of Chemical Technology and Engineering, Department of Catalytic and Sorbent Materials Engineering, Piastów Ave. 42, 71-065, Szczecin, Poland

ARTICLE INFO

Keywords:
H_2 storage
CO_2 capture
Activated carbons
Adsorption mechanism
Narrow micropores
Nutshells

ABSTRACT

Low-cost walnut shell-based carbons with high microporosity were prepared by simple one-step carbonization with chemical activation using KOH, exhibiting the promising potential to be a very good CO_2 and H_2 adsorbent. The physicochemical properties of the obtained carbons were characterized by N_2 and CO_2 adsorption isotherms, X-ray powder diffraction (XRD), Raman spectroscopy, scanning electron microscopy (SEM), Fourier transform infrared spectroscopy (FT-IR), and elemental analysis. The activated carbon AC-800 was characterized by a highly developed specific surface area of 1868 cm^2/g and a high micropore content of 0.94 cm^3/g. It highly exhibited CO_2 uptake in 1 bar was up to 9.54, 5.17, 4.33 mmol/g for 0, 25 and 40 °C, respectively. In addition, the H_2 storage capacity was 3.15 mmol/g at 40 bars. Significantly, confirmed an exceptionally high dependency of CO_2 and H_2 uptake vs micropores structure of activated carbon. AC-800 also shows good selectivity for CO_2/N_2 and fast adsorption kinetics that be easily regenerated with superior cyclic stability after multiple cycles The experimental isotherm data of activated carbon produced from walnut shells were analyzed using Langmuir, Freundlich, Temkin, Sips, and Toth isotherm equations. The fitting details showed that the multitemperature Toth equation is a powerful tool to mathematically represent CO_2 and H_2 isotherms on activated carbon. The easy way of preparation and high capture abilities endow this kind of activated carbon attractive as a promising adsorbent for CO_2 and H_2 storage.

1. Introduction

Progressing climate changes, resulting in extreme weather phenomena, are mainly caused by the emission of greenhouse gases such as methane and carbon dioxide. The latter is the main measure of emissions from industry and the use of fossil fuels [1]. Nowadays, the investigation follows to the need to minimize foreign oil imports, carbon dioxide (CO_2) emissions and climate change, the desire for low- or zero-emission automobiles, and the necessity to store renewable energy sources, and the implementation H_2 as the fuel of the future [2]. Hydrogen energy consumption is not a unique concept, with interest in its practical applications extending back over 200 years [3]. What has changed since the middle of the 1990s is the convergence of variables that makes an economy based on hydrogen energy more alluring. To reduce CO_2 emissions to the atmosphere, adsorption-based systems such as carbon capture and storage are being developed and require careful adsorbent selection. Solid sorbents, particularly activated carbons (ACs), have received a lot of attention in recent years as potential CCS candidates [4,5]. Low cost, excellent surface chemistry, higher surface area, larger pore volume, moisture stability, good chemical and thermal stability, good recyclability, good mechanical resistance, affinity towards CO_2, faster kinetics, and tunable pore structure are the main advantages of ACs [6]. Due to their numerous advantageous properties, ACs are also promising candidates in other fields such as the chemical, food/beverage, environmental, automobile, hydrogen storage, and chemical sectors [7].

Activated carbons can be classified into three types: granular, fibrous and powder, according to the size and shape of the pores [8]. Currently, research involving the use of activated carbon for sustainable purposes is

* Corresponding author.
E-mail address: jaroslaw.serafin@qi.ub.es (J. Serafin).

https://doi.org/10.1016/j.carbon.2022.09.013
Received 2 August 2022; Received in revised form 23 August 2022; Accepted 6 September 2022
Available online 15 September 2022

increasingly encouraged. Activated carbons can be prepared in two ways. The first is the carbonization of the precursor material, which can be the carbonization/pyrolysis of the biomass a, followed by the activation process, which can be chemical or physical [9]. The carbonization or pyrolysis process is responsible for the thermal degradation of the source material, eliminating non-carbonaceous species, in this procedure a rough structure is formed, with little developed pores, which may be clogged by tar, the activation process is intended to improve the quality of these pores, increasing the diameter and consequently the surface area [10]. The activation step can comprise physical and chemical activation. The physical activation process can be performed in two consecutive steps: carbonization of the precursor material at high temperatures (above 300 °C) in an inert atmosphere and thermal activation, at the same temperature or at temperatures higher than carbonization, in the presence of a gas oxidant such as water vapor, carbon dioxide or both [11–13]. These gases promote the oxidation of the carbonaceous material inside the particles, promoting the unclogging of existing pores, and consequently, developing their porous structure [14]. On the other hand, for chemical activation, the material to be activated must be impregnated with chemical substances such as phosphoric acid, potassium hydroxide, sodium hydroxide, zinc chloride, among others, before or after carbonization [15,16]. The chemical activation process can change the structure of the precursor material, resulting in a change in the formation of micropores, mesopores and macropores, where the adsorbents, such as gas molecules, will be allocated. After impregnation by the activating substance, the chemical agent and its decomposition products are removed by washing with water or an acid/base solution, leaving the formed pores free [17].

As many researchers report, in the processes of adsorption of gases such as CO_2 and H_2, the most important role is high microporosity and their surface area [18]. Numerous scientific works have been published regarding the study and improvement of processes and materials used to CO_2 and/or H_2 storage. For example, microporous carbon materials based on biomass corncob [19], pitch mesophase [20], chitosan [21], and potato starch [22], black locust [23], spend dregs [24], peanut shells [25] can present excellent hydrogen and carbon dioxide adsorption capacity.

In this work we present a simple and method of preparation of activated carbons based on biomass from walnut shells. Highly efficient carbon adsorbents were evaluated in terms of texture parameters and CO_2 and H_2 storage performance. The adsorption of a binary mixture of CO_2 and N_2 with composition 15% of CO_2 which can be considered representative of post-combustion capture conditions was assessed at 25 °C and 40 °C. The mechanism of pores formation as a result of chemical activation was explained. The effect of porosity, and in particular microporosity, on gas CO_2 and H_2 adsorption was investigated and their mechanism of adsorption.

2. Materials and methods

2.1. Synthesis of activated carbon from biomass

The walnut shells were grounded, then dried at 105 °C temperature, and prepared as a starting material for obtaining carbon. A saturated KOH solution was used as the chemical activating agent. First, the powder of walnut shells was treated with an activator at ambient temperature for 3 h. The mass ratio of KOH: precursor was 1: 1. Then materials were carbonized under continuous N_2 gas at 18L STP/min. The 500–900 °C carbonization temperature was reached at a 10 °C/min heating rate and was maintained for 1 h. After activation, to prevent oxidation, the sample was cooled inside a furnace under N_2 gas flow. After cooling, the resulting product was washed with distilled water, then with 1 mol/dm^3 hydrochloric acid and again with distilled water until the pH was neutral. The resulting material was finally dried in an oven at 200 °C overnight. The schematic preparation of walnut shell activated carbon is shown in Fig. S1.

2.2. Materials characterization

To evaluate the textural properties of the prepared samples were analyzed using N_2 adsorption-desorption at −196 °C and CO_2 at 0 °C. Gas adsorption measurements were carried out on a QUADRASORB evo ™ volumetric apparatus. Before adsorption measurements were taken, the samples were degassed durning 16h under vacuum at 250 °C. To determine specific surface area (S_{BET}) the Brunauer-Emmett-Teller (BET) equation was used in the relative pressure range of 0.05–0.25. The total pore volume (TPV_{N2}) was calculated from N_2 adsorption isotherms at the highest relative pressure ($P/P_0 = 0.99$). Non-local density functional theory (NLDFT) model was used to determine the porosity of a sample – pore size and pore size distribution. The NLDFT method use a classical fluid density functional theory to construct the adsorption isotherms in ideal pore geometries (e.g., N_2 adsorption in the slit-pore model at 77 K). This model used to estamitaed pore size distributions from N_2 (MPV_{N2}) and CO_2 (MPV_{CO2}) adsorption isotherms. The X-ray diffraction (XRD) analysis of the prepared ACs were recorded by an X-ray diffractometer (PANalytical Empyrean) using Cu Kα radiation (λ = 1.54056 Å), as the radiation source in the 2θ range of 20–80°. Determination of the activated carbon spectra was carried out using a Fourier transform infrared spectrometer from The Digilab Division of Bio-Rad (Cambridge, MA, USA), model FTS-175 C. The research was carried out using the transmission method, using the technique of pressing samples with potassium bromide. The carbon samples were mixed with KBr at a constant activated carbon weight to KBr weight ratio of 0.25% and pelleted at a pressure of 5 bar. The advantage of using KBr pellets is that there are no KBr bands in the spectrum in the measuring range 4000–500 cm^{-1}. The Raman spectra was used to determine the quality of the obtained activated carbon. The analysis was performed using a Renishaw InVia Raman Microscope spectrometer with excitation laser with a beam length of 785 nm. Morphologies of the ACs were examined using scanning electron microscopy (SEM) with cold emission (UHR FE-SEM Hitachi SU8020). For elemental analysis in activated carbons was carried out with elemental analyzers (LECO Corporation). For potassium quantity analyze XRF (The X-ray fluorescence energy dispersion spectrophotometer (EDXRF) of the Epsilon 3 type from PANalytical B. The CO_2 adsorption equilibrium of all carbon adsorbents were obtained on a Quantachrome Instruments QUADRASORB evo™ gas volumetric analyzer. The adsorption process was carried out at two temperatures 0 °C (ice-water bath), 25 °C and 40 °C (circulating water bath) at pressure up to 1 bar using pure CO_2. Before the adsorption analysis, each sample was pretreated at 200 °C for 16 h under vacuum to desorb any moisture and then cooled down to the required temperature, followed by ultrahigh purity CO_2 into the system. H_2 adsorption at a pressure higher than 1 bar was tested by the volumetric method, using the Hiden Isochema IMI apparatus. H_2 adsorption measurements were made for the temperature of 25 °C and the pressure up to 40 bars. An appropriate mass of the sample was poured into the reaction tank, with a volume of about 2 cm^3. To reduce the unused volume, the remaining space of the reaction vessel was filled with glass wool. After closing, the entire system was flushed with helium to check system for leaks. The next step was to degases the sample at 250 °C. After the degassing was completed, the adsorption isotherms were measured.

2.3. Modeling of adsorption isotherms

To identify the resulting adsorption complex on the adsorbent surface when the adsorption process reaches an equilibrium state, it is significantly crucial to determine the appropriate mechanisms that take place during the process. Therefore, the subsequent interpretation of the data obtained from the isotherm models is necessary to predict the nature of the adsorption and the effective design of the adsorption system [26]. In view of that, five selected equilibrium models were used to analyze the experimental CO_2 adsorption data on activated carbon, which are two-parameter (Langmuir, Freundlich, Temkin) and

Table 1
Non-linear equations of selected isotherm models.

Isotherm model	Nonlinear form of equation	Parameters	Adsorption mechanism	References
Langmuir	$q_e = q_m \frac{K_L \cdot P}{(1 + K_L \cdot P)}$	q_m - maximum adsorption capacity (mmol/g) P– relative pressure of the adsorbate (bar) K_L - Langmuir isotherm constant (bar^{-1})	Monolayer adsorption on a homogeneous surface	[27,28, 29]
Freundlich	$q_e = K_F \cdot P^{\frac{1}{n_F}}$	K_F - Freundlich isotherm constant (bar^{-1}) P - relative pressure of the adsorbate (bar) $1/n_F$ – heterogeneity factor n_F – Freundlich exponent	Monolayer or multilayer adsorption on a heterogeneous surface.	[27,28, 30]
Temkin	$q_e = \frac{R \cdot T}{b_T} \cdot \ln(K_T \cdot P)$	b_T - Temkin isotherm constant related to the heat of adsorption (J/mol) R- universal gas constant (J/mol·K) T- temperature (K) K_T - Temkin isotherm equilibrium binding constant (bar^{-1}) P– relative pressure of the adsorbate (bar)	Adsorption on a heterogeneous surface accounts for indirect interaction between the sorption complex at a wide pressure range.	[27,28]
Toth	$q_e = \frac{q_m \cdot K_T \cdot P}{[1 + (K_T \cdot P)^{n_T}]^{\frac{1}{n_T}}}$	q_m - maximum adsorption capacity (mmol/g) P– relative pressure of the adsorbate (bar) K_T - Toth isotherm constant (bar^{-1}) n_T – heterogeneity factor	Adsorption on heterogeneous surface at both low and high pressure.	[27,28, 31]
Sips	$q_e = \frac{q_m \cdot (K_S \cdot P)^{\frac{1}{n_S}}}{1 + (K_S \cdot P)^{\frac{1}{n_S}}}$	q_m - maximum adsorption capacity (mmol/g) P– relative pressure of the adsorbate (bar) K_S - Sips isotherm constant (bar^{-1}) n_S – Sips isotherm exponent	Combined form of Langmuir and Freundlich model.	[27,28, 32]

three-parameter (Toth, Sips) isotherm models. The non-linear form of isotherm equations, their theoretical assumptions, and description of parameter are presented in detail in Table 1. In the scoping of these studies, other isothermal models could potentially be implemented and considered that include: Radke-Prausnitz, Hill-Deboer, or Fowler-Guggenheim models.

To determine the model that most accurately reflects the interaction between the adsorbent and the adsorbate, all five isotherms models were fitted to empirical data using nonlinear regression using the Solver Add-in in Excel and additionally verified by Origin's NLfit tool. Linear regression was rejected in the analysis due to the potential inherent bias resulting from the transformation of the original equation (non-linear), which could lead to inaccuracies in the isothermal parameter estimate as well as to distortion of fits [33]. On the contrary, nonlinear regression gives a theoretically precise method, where it offers an exact fit of the predicted value of the isotherm model to the experimental data, mainly based on minimization of the error distribution between them [34].

The best fitting between the selected theoretical model and the experimental isotherm data was evaluated using the sum of the squares errors (ERRSQ/SSE), which is the most frequently used error function in modeling of adsorption isotherms. ERRSQ is calculated by the difference in squares between the experimental and model data. Moreover, it is also worth noting that this error should be applied for lower pressures or concentrations of the adsorbate. The ERRSQ error is defined by the following equation [35]:

$$\mathrm{ERRSQ} = \sum_{i=1}^{n} \left(q_{e,exp} - q_{e,mod}\right)^2 \quad (1)$$

Where:

$q_{e,exp}$ - experimental amount of adsorbed adsorbate [mmol/g].
$q_{e,mod}$ - calculated amount of adsorbed adsorbate [mmol/g].

3. Results and discussions

3.1. Studies of textural properties by the adsorption of N_2 at temperature of −196 °C and CO_2 temperature of 0 °C

N_2 adsorption isotherms at −196 °C on activated carbons obtained in the temperature range of 500–900 °C are shown in Fig. 1. The isotherms show high N_2 adsorption at low relative pressure, which is characteristic of microporous materials. High N_2 adsorption at low relative pressure

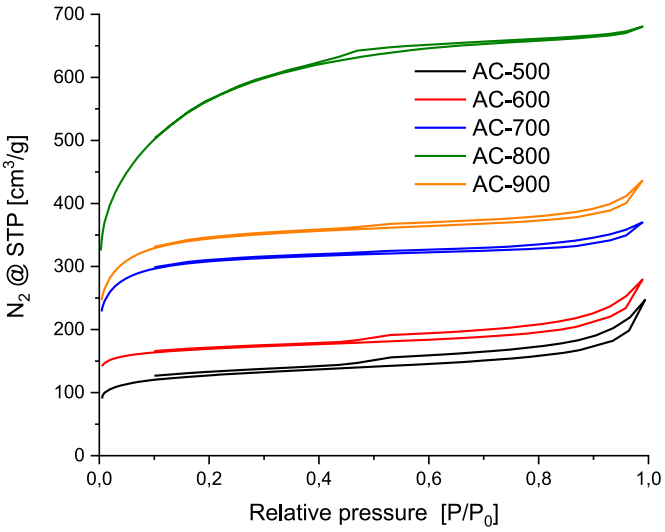

Fig. 1. Nitrogen adsorption-desorption isotherms at − 196 °C of the prepared activated carbons. (A colour version of this figure can be viewed online.)

(less than 0.1 P/P_0) indicates the availability in the carbons of a large volume of micropores with a narrow pore size distribution. It was noticed that the nitrogen adsorption capacity in −196 °C clearly increased for the carbon samples with the increase of the thermal treatment temperature during their preparation, reaching the highest value for the sample obtained at 800 °C. From the point of view of the IUPAC [30]classification, the nitrogen sorption isotherms in the initial range of relative pressure P/P_0 corresponded to type Ib, and in the range of medium and higher pressures to type IV. The Ib isotherm type is characteristic for materials with narrow micropores, where the filling of micropores is the dominant mechanism at low P/P_0 [30] On the other hand, a characteristic feature of type IV isotherms is the occurrence of a clearly formed hysteresis loop related to the phenomenon of capillary condensation in the area of mesopores. The presented isotherms contain a hysteresis loop of H4 type around the pressure P/P_0 of about 0.45, resulting from capillary condensation of nitrogen in mesopores [31]. This indicates that these carbons, apart from relatively well-developed microporosity, also have a developed mesoporosity. The obtained activated carbons were characterized by the specific surface area ranging from 406 to 1868 cm^2/g (Table 2).

Table 2
Textural properties of walnut shells activated carbons.

Samples	Yield content [%]	BET (m^2/g)	TPV_{N2} (cm^3/g)	MPV_{N2} (cm^3/g)	MPV_{CO2} (cm^3/g)
500	49	406	0.38	0.31	0.36
600	42	528	0.43	0.36	0.35
700	38	958	0.57	0.50	0.62
800	35	1868	1.06	0.94	0.55
900	27	1077	0.68	0.57	0.23

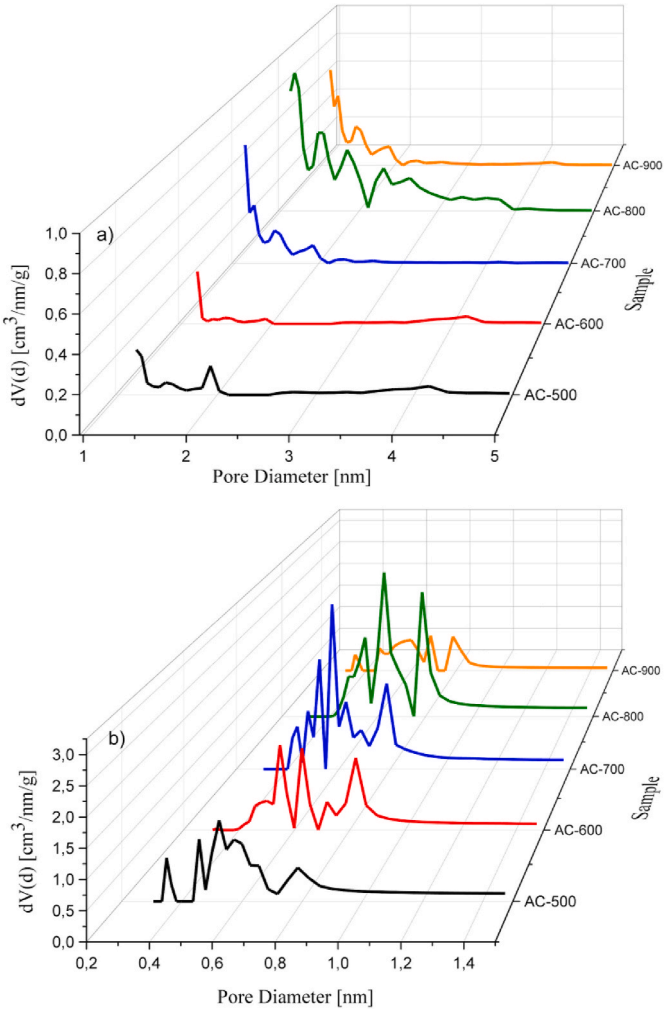

Fig. 2. PSDs of the activated carbons prepared at different activation temperatures (a) based on N_2 sorption, (b) based on CO_2 sorption. (A colour version of this figure can be viewed online.)

Based on the analysis of the pore volume distribution, information on the structure of the tested adsorptive materials was obtained. In order to investigate the relationship between the pore size of the carbons and the temperature of the preparation process, an analysis of the pore size distribution of the obtained activated carbons was performed. It was found that for the tested carbons a similar pore distribution was observed. All carbons, apart from micropores, also contained mesopores with sizes from 2 to 3 nm. Fig. 2a shows the pore size distribution determined by the DFT method from N_2 adsorption measurements at −196 °C. The highest proportion of micropores in the range from 1.4 to 2 nm was found in carbon AC-800, which was also characterized by the highest proportion of mesopores up to 4 nm. No mesopores with diameters greater than 5 nm were observed. Fig. 2b shows the distribution of pores with a diameter of 0.3–1.4 nm determined by the DFT method based on CO_2 adsorption at the temperature of 0 °C for the tested carbons. Several intense peaks were found with diameters of approx. 0.4–0.5 nm, 0.5–0.7 nm and 0.8–0.9 nm. These peaks occurred in all materials, regardless of the temperature of their preparation. It was found that pores with a diameter of 0.5–0.7 nm were dominant in the AC-700 and AC-800 carbons. On the other hand, pores with a diameter of 0.8–0.9 nm predominated in the AC-800 carbon. The numerical values are summarized in Table 2.

Results of the porosity presented in Table 2 is attributed to the efficient chemical activation by KOH. As proven mechanism of activation using KOH as activated agent begin by transformation of KOH at 300 °C [32]:

$$6KOH + 2C \rightarrow 2K + 3H_2 + 2K_2CO_3 \quad (2)$$

As the carbonization temperature increases, K_2CO_3 decomposes:

$$2K_2CO_3 + 2C \rightarrow 2K + 3CO \quad (3)$$

Thus, during the activation process, a number of changes occur in the material, such as: chemical etching via redox reactions, gasification of carbon, intercalation of potassium products resulting in lattice expansion which upon hydrochloric acid washing gives a highly porous carbon framework [36].

The pore formation mechanism begins with the surface of the material, where the KOH reacts with C. As a result, in the first phase, the formation of mostly small pores, characterized by a relatively small diameter, are micropores and mesopores (Fig. 3-I). When the temperature rises around 500 °C, transverse pores are formed (Fig. 3-II). With the subsequent increase in temperature up to 750–800 °C the reactions rate with carbon and the diffusion rate of the reagents increased. There is a significant pattern in the formation of transverse pores and their branching (Fig. 3-III). At 800C-900 °C, the surface area is reduced, pores continue to form micropores, but the process of increased mesopore formation also begins (Fig. 3-IV). Increasing the carbonization temperature above 900 °C would result in the destruction of the microporous structure and the formation of wide macropore pores (Fig. 3-V) [37]. Understanding and defining the mechanism of pore formation is an important turning point in the preparation of activated carbons with the desired properties.

The yield of activated carbon is usually defined as the final weight of activated carbon produced after activation, washing, and, divided by the initial weight of raw material, both on a dry drying basis according to equation (4) [38]:

Fig. 3. The variation of pore structure formation through chemical activation in activated carbon. (A colour version of this figure can be viewed online.)

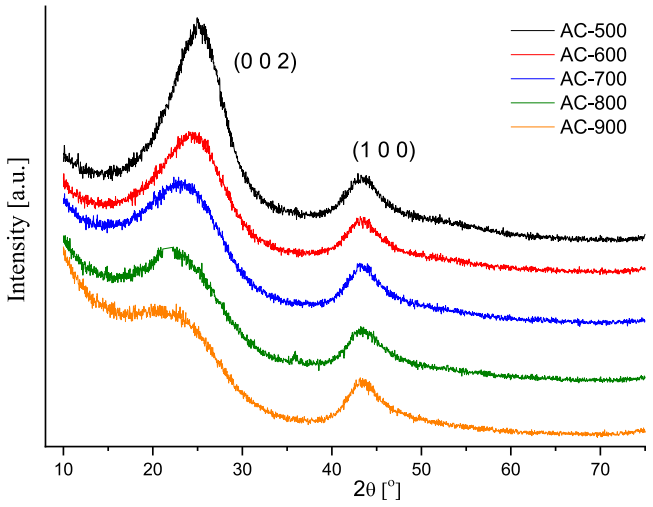

Fig. 4. XRD analysis of activated carbons. (A colour version of this figure can be viewed online.)

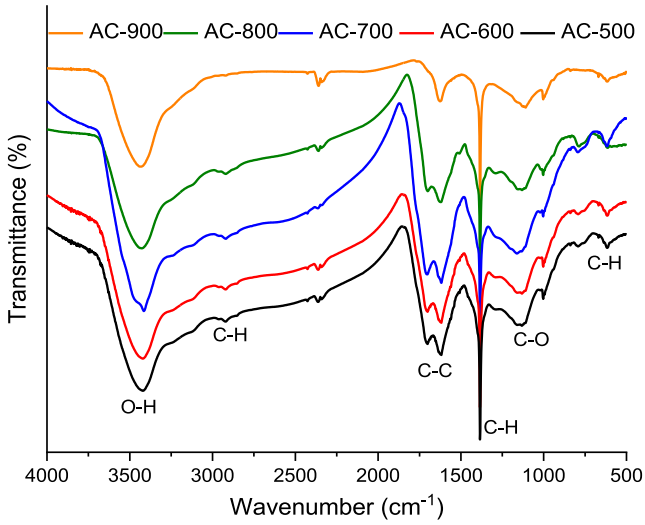

Fig. 5. FT-IR pattern of activated carbons. (A colour version of this figure can be viewed online.)

$$Y\ content(\%) = \frac{m}{m_0} x\ 100 \quad (4)$$

Where:

m and m_0 are the dry weight of final activated carbon (g) and dry weight of precursor (g), respectively.

The activated carbon yield content ranged from 27 to 49% (Table 2). Similar results of the yield content range were obtained by other authors: peach stones, 42–44% [39], palm oil shells, 27–64% [40], coconut shells, 49–52% [41].

3.2. XRD method

XRD pattern of 500–900 °C carbons are shown in Fig. 4. XRD profile shows that all materials are low crystalline. The diffraction patterns show only two-digit broad diffraction peaks located at approx. 24° and 44°, which correspond to (0 0 2) and (1 0 0) plane in non-graphitic disordered carbon structure, respectively [42–44]. The low intensity of the peak corresponding to the plane (1 0 0) at approx. 44° for activated carbons shows the disordered graphite structure that was formed for the activated carbons [42]. Similar diffractograms of poorly available carbon materials can be achieved in the works [44,45], in which the authors attribute them to amorphous carbons.

3.3. FT-IR spectroscopy

The FT-IR spectra of the carbons are presented in Fig. 5. The FT-IR analysis showed that the characteristic peaks for all samples are basically the same and showed vibrations mainly in the area of 3400–3500, 2900–3000, 1650–1700, 1375–1400, 1000–1100 and 600-800 cm^{-1}. A strong diffraction peak at 3420 cm^{-1} corresponds to the tensile vibration of O–H bond, which may be caused by dehydration of the precursor in the activated carbon preparation process [46,47]. The band at 2930 cm^{-1} corresponds to C–H asymmetric stretching vibration, while the vibration peaks appearing around 1627 and 1700 cm^{-1} can be attributed to the stretching vibrations of the C═C bond [48]. The 1390 cm^{-1} band represents in plan C–H bending [42]. The bands at 1000 and 1100 cm^{-1} corresponds to C–O stretching vibration. The vibration peak appearing near 800-600 cm^{-1} belong to the peak of bending out of the plane C–H [48]. The infrared spectrum of the tested activated carbons has a shape similar to the spectra recorded for lignocellulosic materials [42,48].

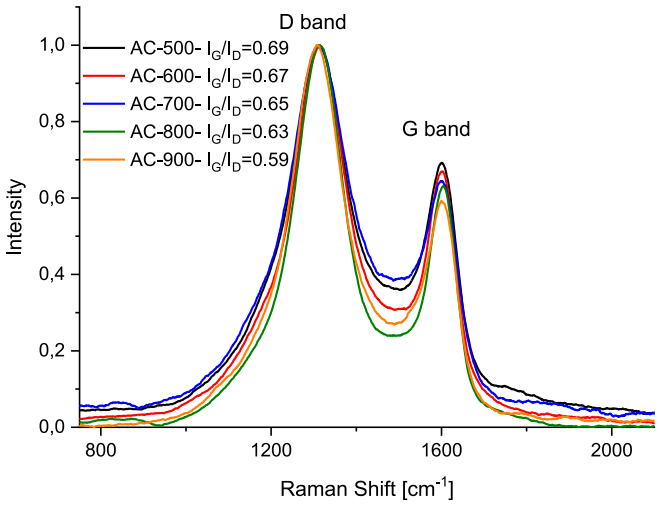

Fig. 6. Raman spectra of activated carbons. (A colour version of this figure can be viewed online.)

3.4. Raman spectroscopy

Raman scattering spectra exhibit two broad Raman bands: the first peak detected in the range of 1315 cm^{-1} can be assigned to the defect or disordered phase (D-band), and the second peak at 1601 cm^{-1} can be attributed to the graphitic phase (G-band) of carbon (Fig. 6). The D-band represents the vibrations of carbon atoms having a dangling bond in the terminations of the disordered graphite structure, whereas the G-band represents the stretching vibration mode of the sp^2 hybridized carbon atoms in the graphite layer [49,50]. The ratio of the intensities of D-band and G-band (I_G/I_D) measures disorder in carbon materials with the graphitic structure (number of sp^2 clusters). The I_G/I_D increases with the decrease in crystallinity indicating that the chemical activation process led to more defects appearing in the samples. The carbon samples exhibited I_G/I_D ratios in the range of 0.59–0.69. Careful observations reveal that the I_G/I_D ratio decreases from 0.69 to 0.59 upon the increase in the temperature of carbonization indicating more and more defects in the carbon framework and demonstrating an increase in the graphitic carbon.

3.5. SEM method

The surface morphology of activated carbons was examined using the scanning electron microscopy technique. Walnut shell carbons showed a uniform structure with a predominance of macropores, which had an average diameter of 12 μm [51]. The carbon-KOH interaction creates a huge number of micropores, which considerably increases the surface area and volume of the pores, according to an examination of the microstructure of activated carbon [52]. As seen in Fig. 7., the activated carbon created in this study may take on a variety of shapes with different pore sizes, wall thicknesses, and shapes. A significant amount of organic material was removed, and pores were created because of the activation process. The SEM pictures of the AC-500, AC-600, AC-700, AC-800, and AC-900 are displayed in Fig. 7. The micrographs show that each sample had hollow tunnels throughout, which is indicative of the gasification of volatiles after activation. All the AC samples were made up of agglomerated high-quality particles. Additionally, it was possible to see that all sample's carbon particles were disordered, which was consistent with the findings of the XRD study [53].

3.6. The elemental analysis

The elemental analysis results of the activated carbons obtained at various activation temperatures are shown in Table 3. It was observed that with increasing temperature of carbonization all carbon samples characterized of higher contents of C and lower contents of H and O. This means that chemical activation involving potassium hydroxide led to accelerate the removal of H and O and this resulted in an increased C. With an increase in the activation temperatures from 500 to 900 °C, the carbon content of the activated carbon samples was increased from 70.46 to 96.35 wt%. Moreover, the hydrogen content decreased from 2.78 to 0.74 wt%, And similar trend was observed for the oxygen content, decreasing from 25.21 to 2.16 wt%. Changes of the elementary content result from the release of volatiles during carbonization that resulted in the elimination of non-carbonaceous parts and enrichment of carbon element [54]. The obtained results of the elemental analysis for activated carbons from walnut shells are similar to other activated carbons obtained from the research biomass [55–57]. Potassium content was also determined using the XRF method. All activated carbons had trace amounts of potassium not exceeding 0.06% wt. The obtained results showed that by washing with water and 1 M HCl, potassium compounds and metallic potassium, which intercalated in the carbon structure, were practically removed from the activated carbons, and a small residue is most likely related to its incorporation into the activated carbon matrix along with the carbonization process.

3.7. Studies on CO_2 and H_2 adsorption

Walnut shell-based activated carbons were tested for their ability to adsorb CO_2 at three temperatures 0 °C, 25 °C and 40 °C at a pressure of 1 bar. As can be seen in Fig. 8., the system of isotherms for all activated carbons shows that at low adsorbate concentrations, when most of the

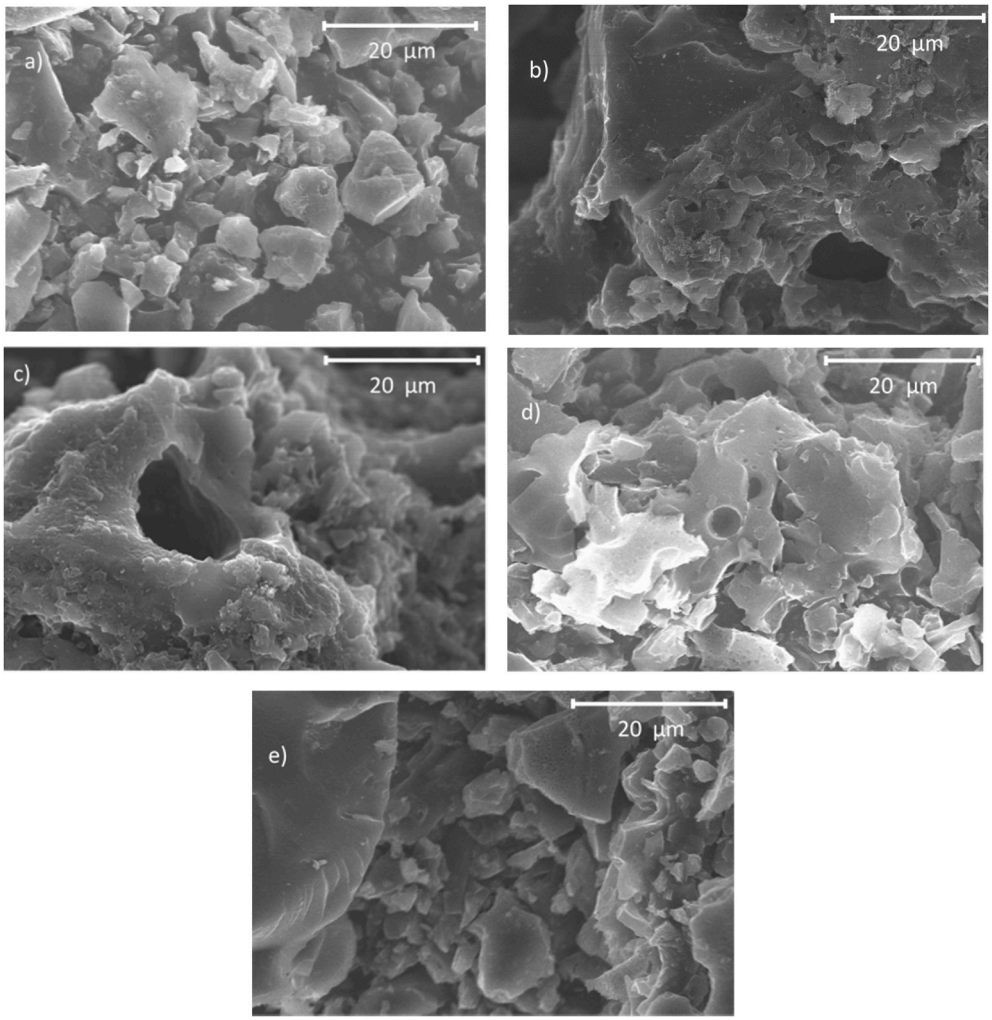

Fig. 7. The SEM images of activated carbons a) AC-500; b) AC-600, c) AC-700; d) AC-800; e) AC-900. (A colour version of this figure can be viewed online.)

Table 3
Elemental analysis of activated carbons.

Sample	Elemental analysis			
	C [wt%]	H [%]	N[%]	O[%]
AC-500	68.46	2.58	1.75	27.21
AC-600	75.71	2.05	1.51	20.73
AC-700	84.24	1.53	1.42	12.81
AC-800	91.88	0.98	0.98	6.16
AC-900	96.35	0.74	0.75	2.16

adsorbent sites are not bound to the adsorbate molecules, adsorption is very easy and some of the molecules are adsorbed. As the adsorbent surface is covered with adsorbate particles, the number of adsorption centers not associated with the adsorbate decreases. The AC-800 sample had the highest adsorption capacity, amounting to 10, 5, 4.5 for 0 °C, 25 °C and 40 °C, respectively. The obtained CO_2 adsorption values for AC-800 are among the highest when compared to other activated carbons obtained by other researchers, summarized in Table 4.

To understand the mechanism of CO_2 adsorption (Fig. 9a), we determined the dependence of CO_2 adsorption on the total specific surface area (Fig. S2a), the total volume of pores (Fig. S2b), the volume of micropores determined by the N_2 isotherm (Fig. S2c) and the volume of micropores determined by the CO_2 isotherm (Fig. S2d). When comparing the R^2 correlation coefficients, the highest values were obtained for the relationship between CO_2 adsorption and the volume of micropores determined using CO_2, it was $R^2 = 0.75$ for 0 °C, $R^2 = 0.87$ for 25 °C and $R^2 = 0.90$ for 40 °C. The process of adsorption at low pressure uptake mainly depends on the volume of narrow micropores instead of the specific surface area and total pore volume. The adsorbent-adsorbate interaction energy, which comes from short-range attractive and repulsive forces, is notably reinforced when the adsorption occurs in extraordinarily small pores due to the overlapping of potential fields from neighboring walls. The enhanced adsorption potential, therefore, results in the complete filling of small micropores at low relative pressure (<0.01). For that reason, the adsorption mechanism consists of volume-filling rather than surface cover typical of meso/macroporous materials and the adsorbates occupying these small micropores are in a liquid-like state [75,76]. Therefore, the interaction between adsorbents and CO_2 molecules becomes stronger when the pore size decreases. Thus, it can be concluded that narrow micropores are ideal sites for CO_2 sorption to occur.

The essential is that H_2 storage capacity is governed by the factors that influence the adsorbate – adsorbent interactions. In porous materials such as activated carbon the most important factors in determining adsorptive H_2 uptake are surface area and micropore volume [89,90]. Generally, the mechanism for H_2 storage (Fig. 9b) by means of physisorption is the van der Waals attraction between the surface of the ACs and the H_2 molecules [91]. Nevertheless, the van der Waals interaction between the H_2 molecules is weak; therefore, to expect a few layers of hydrogen packing onto an adsorbent surface is impractical [92]. As with CO_2 adsorption, presence of an adequate volume of small pores is key factor that attributes to H_2 uptake. In order to increase the interaction energy between H_2 molecules and the carbon adsorbent, narrowing the pore size due to overlap of the potential fields from both sides of the pore wall to a degree determined by the pore width [93]. In the case of smaller pores, the overlap of van der Waals potentials due to the atoms of the adjacent walls favors stronger physisorption. Finally, the total interaction between the adsorbate molecule and a solid is greater if the molecule can interact with a larger number of surface atoms, as what happens in small pores [94]. For that reason, smaller pores are more efficient in H_2 storage due to stronger interaction with H_2 molecules, as confirmed by the analysis of H_2 uptake dependence as a function of (a) BET surface area (Fig. S3a), (b) total pore volume (Fig. S3b), (c) VmN_2 (Fig. S3c) and (d) $VmCO_2$ (Fig. S3d) [95]. The best correlation coefficient R^2 was achieved for micropores up to 1.4 nm and it was $R^2 = 0.89$.

Fig. 10 present the H_2 adsorption isotherms on activated carbon samples at temperature of 25 °C. The best result was obtained for the sample AC-800 equal 3.15 mmol/g at 40 bars. The walnut shells based activated carbon obtained in this study and its ability to store hydrogen may constitute a concretion for other available carbon materials used in this process, as presented in Table 5.

3.7.1. Isosteric heat of adsorption

The isosteric heat of adsorption (Qiso) value is important to characterize the interaction between the adsorbent and the adsorbate. Provides information on the strength of adsorption. A higher value of the isosteric heat of adsorption indicates a stronger interaction between the adsorbate and the adsorbent. The high isosteric heat of adsorption causes a high cost of regeneration. The isosteric heat of adsorption is expressed by the Clausius-Clapeyron equation:

$$Q_{iso} = -R\left(\frac{\partial \ln(p)}{\partial\left(\frac{1}{T}\right)}\right)_{\theta} \quad (5)$$

where:

Q_{iso} – is the isosteric heat of adsorption at a constant surface coverage θ [kJ/mol]
R – universal gas constant [J/mol·K]
θ – a surface coverage degree

The isosteric heat adsorption values for activated carbons changed from 28 to 32 kJ/mol for surface coverage in the range of 0.1–0.35 (Fig. 11). In the case of adsorption type determination, when the isosteric heat of adsorption value is lower than 80 kJ/mol, there is talk of physisorption, while for chemisorption it is in the range of 80–200 kJ/mol [96]. The obtained values clearly confirm the physical nature of CO_2 sorption on activated carbons. The isosteric heat of adsorption decreased with the coverage of the surface. The greater the surface coverage, the weaker the interaction between carbon dioxide and activated carbon. Carbon dioxide is bound to the surface of the activated carbons by van der Waals forces and can be easily desorbed. Recent studies show that if the gas contains only CO_2, the most advantageous are sorbents with an isosteric heat of CO_2 adsorption within the range of 22–28 kJ/mol. On the other hand, sorbents for CO_2 adsorption from flue gases should be characterized by the heat of CO_2 adsorption from 26 to 31 kJ/mol [97]. As seen in this case, the values of isosteric heat of CO_2 adsorption obtained in this study for all walnut shell activated carbons met these requirements. It is noteworthy that such values are highly desirable because of the low regeneration costs.

3.8. Studies modeling isotherms

3.8.1. Adsorption isotherms

The experimental equilibrium data on CO_2 uptake by activated carbon (AC) with best-fit isotherm model curves for temperatures ranging from 0 °C to 40 °C are presented in Fig. 8. It has been observed that the tested AC samples possess an adsorption capacity between 3.55 and 9.59, 2.19–5.18, and 1.43–4.34 mmol/g for three adsorption temperatures. The AC sample synthesized at an activation temperature of 800 °C exhibits the highest CO_2 uptake with excellent gas adsorption properties (9.59 at 0 °C and 1 bar) in the region of low pressure. In the case of H_2, adsorption equilibrium test was carried out for 25 °C. The AC-800 sample also stands out for the highest adsorption capacity, reaching 3.15 mmol/g at 25 °C and 1 bar. The fact suggests that AC-800 has the most highly developed micro- and mesoporous structure than any other sample. On the contrary, AC-500, AC-600, AC-700, and AC-900 have H_2 uptake of 1.22, 1.39, 2.06 and 0.92 mmol/g under the same conditions, respectively. In a similar vein to CO_2, Fig. 9 depicts the variation of H_2

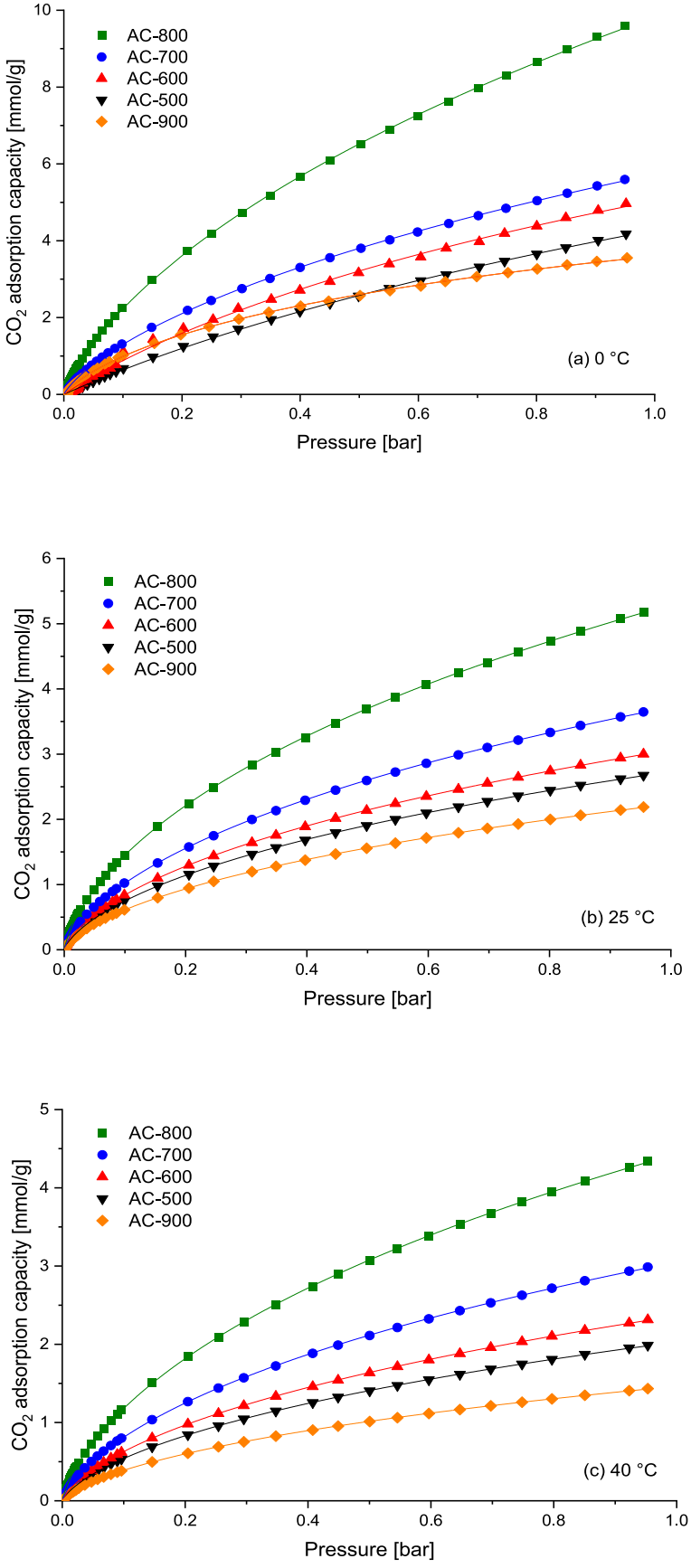

Fig. 8. The CO_2 adsorption isotherms on AC samples at temperature of (a) 0 °C, (b) 25 °C, (c) 40 °C. Points represent experimental data; lines reflect Toth's isothermal model. (A colour version of this figure can be viewed online.)

Table 4
CO_2 adsorption capacities at 0, 25, 40 °C and different pressures for carbon materials presented within the literature.

Carbon Source	0 °C (mmol/g)	25 °C (mmol/g)	40 °C (mmol/g)	Ref.
Bean dreg	–	4.24	–	[58]
Packaging Waste	5.33	4.20	–	[59]
Walnut shell	–	–	1.05	[60]
Starch	7.49	3.84	–	[61]
Cross-linked polymers	6.95	–	–	[62]
3D-Printed Monoliths	–	–	3.17	[63]
surgical mask waste	3.90	–	–	[64]
Pine Nutshell	7.70	5.0	–	[65]
Rice Husk	6.24	3.71	–	[66]
Waste CDs and DVDs	5.80	3.30	–	[67]
Pinus canariensis cones	6.40	–	–	[68]
Coconut Shell	7.00	5.00		[69]
Argan Fruit Shell	–	5.63	–	[70]
Rice Husk	7.55	–	–	[71]
Common Polypody	9.05	5.67		[72]
Paulownia sawdust	8.00	—	–	[73]
Organic polymer	7.60	–	–	[74]
Walnut Shell	9.56	5.17	4.34	This work

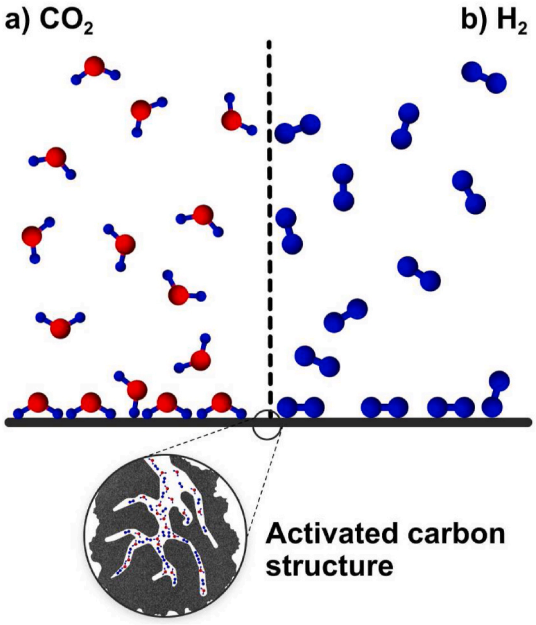

Fig. 9. Schematic visualization of adsorption mechanism a) CO_2 and b) H_2. (A colour version of this figure can be viewed online.)

adsorption experimental data with the equilibrium pressure and the best correlating isothermal model curve.

The shape of all CO_2 and H_2 adsorption isotherms on activated carbon is monotonically concave, and, as a result, they can be classified as type I according to the IUPAC classification (description of microporous adsorbents) [98]. Empirical point analysis indicates that the amount of adsorbed CO_2 in the equilibrium state decreases with increasing temperature, analogous to the exothermic nature of adsorption, indicating that the process is carried out more favorably at lower temperatures. It may suggest the physical adsorption phenomenon, which involves van der Waals forces that compared to the kinetic forces of CO_2 molecule collisions, become negligible as the temperature increases (the strength of the binding forces between CO_2 and a surface od adsorbent is

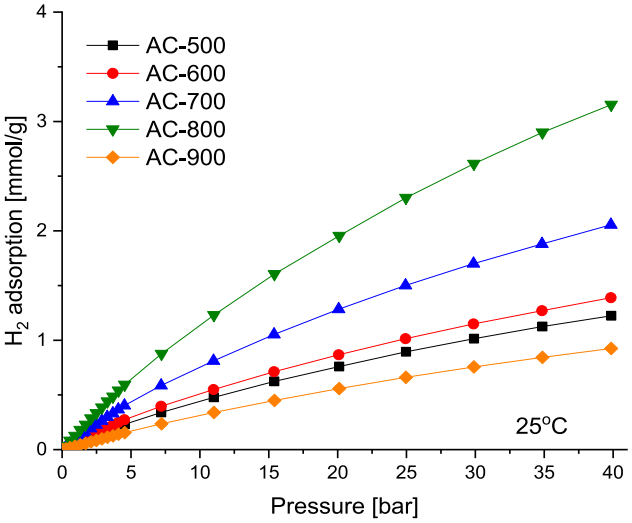

Fig. 10. The H_2 adsorption isotherms on AC samples at temperature of 25 °C. Points represent experimental data; lines reflect Toth's isothermal model. (A colour version of this figure can be viewed online.)

Table 5
H_2 storage capacities at 25 °C and different pressures for carbon materials presented within the literature.

Carbon Source	Pressure (bar)	H_2 (mmol/g)	Ref.
Amorphous cellulose	80	1.70	[77]
anthracite	20	1.15	[78]
Olive Bagasse	200	3.15	[79]
Corncob	50	2.20	[80]
Almond Shells	50	1.55	[81]
Mandarin Fruit	25	2.25	[82]
Viscose rayon cloths	20	0.85	[83]
Cellulose Acetate	20	0.50	[84]
Wood Chips	80	2.75	[85]
Sucrose	100	2.95	[86]
Polymeric precursors	100	2.00	[87]
Polyaniline	80	3.00	[88]
Walnut Shells	40	3.15	This work

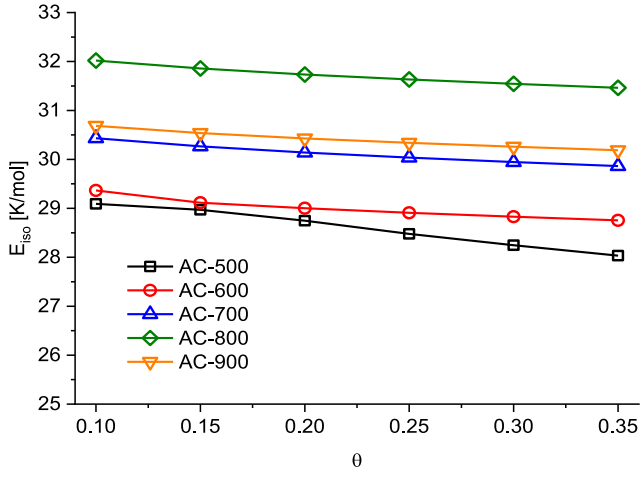

Fig. 11. Isosteric heat of adsorption plots of CO_2 adsorption.

weakening). Moreover, as expected, the rise in the partial pressure as a driving force (pressure gradient) for adsorption causes an intensification of the adsorption capacity of CO_2 at all temperatures, as a consequence

of exothermicity. For H_2, such broad and in-depth observations cannot be made due to the single-temperature adsorption study, however, the increase in pressure also intensifies the uptake and the process can be considered exothermic.

3.8.2. Fitting results of isotherm models

The calculated sum of squares error (ERRSQ) values from fitting the following isotherm models, such as Langmuir, Freundlich, Temkin, Toth, and Sips, which were discussed earlier are included in Table S1 and Table S2. To contrast the accuracy of different models, each models ability has been examined to effectively minimize an objective error function. Statistical investigation and selection of the smallest ERRSQ values allowed the choice of the model with the minimum distribution of discrepancies between the experimental and model data of CO_2 and H_2 adsorption on AC. According to this error function, the Langmuir, Freundlich, and Temkin models are not as suitable as other models to characterize CO_2 and H_2 adsorption on any of the AC samples that were tested. The Toth and Sips models seem to be the most feasible choice for predicting the findings by non-linear regression, which are consistent with the adsorption isotherms that were experimentally determined. However, the Toth model, which is an empirical modified form of the Langmuir equation involving an asymmetric quasi-Gaussian distribution of adsorption sites [99], has a greater degree of congruence with the experimental data in the entire range of adsorption temperatures. Its ERRSQ values for CO_2 are in the range: 0.0250 to 0.2222, 0.0009 to 0.0053, 0.0004 to 0.0041, correspondingly for the increasing temperature of adsorption. At the same time, for H_2 these values oscillate between 0.000099 and 0.0008. Therefore, collated to the Sips models, the non-linear Toth equation is better able to accurately characterize the CO_2 and H_2 adsorption isotherms over the AC and was the only one used to demonstrate the quality fit. To contrast the fitting of other isothermal model curves to the Toth, their runs are demonstrated for CO_2 and H_2 adsorption on AC-800 at 0 and 25 °C (Fig. 12, Fig. 13). As it can be seen from, the modeling isotherm with Toth and Sips nonlinear equation yields competitive prediction to the experimental isotherms than the Langmuir, Freundlich, and Temkin fittings, where their curve ran along the experimental points in the whole range of pressures. The obtained results of modeling non-linearized isothermal equations allowed the following model classification (from the left the best-fit model), for CO_2:

$0°C \quad Toth > Sips > Langmuir > Freundlich > Temkin$

$25°C \quad Toth > Sips > Freundlich > Langmuir > Temkin$

$40°C \quad Toth > Sips > Freundlich > Langmuir > Temkin$

while for H_2 at 25 °C:

$Toth > Sips > Freundlich > Langmuir > Temkin$

The parameters of all isotherm models are presented in Table S3 and Table S4. Interpreting the ones for the best-fitted model is a particularly important stage, which allows correct recognition of the nature and mechanism of adsorption on the surface of AC. The parameter of maximum CO_2 adsorption capacity (qm), according to the Toth model, decreases with the growth of the adsorption temperature growth, which confirms that the phenomenon of CO_2 adsorption in activated carbon is an exothermic process, as noted earlier. It was found that their values for all set samples at 0, 25, and 40 °C are roughly around: 12.032–184.745, 43.079–102.029 and 26.575–80.542 mmol/g. The analysis of the maximum H_2 adsorption capacity parameters correlate with earlier observations and reflects the adsorbed amount of gas in the equilibrium state (3.236–15.443). The results indicate that the model values are quite comparable to the measured ones. In the case of Toth constant (affinity parameter) values, they vary between 0.387 and 1.840, 0.009–0.011 bar^{-1} for CO_2 and H_2, respectively.

To explore more thoroughly the presence of diverse chemical and structural qualities on the AC surface, the main assumptions of the Toth model are crucially needed. The Toth model is especially helpful for characterizing adsorption on the heterogeneity surface of porous adsorbents in the gas phase [100] that satisfies both the low and the high boundary of the adsorbate concentration. When the n_T parameter measuring surface heterogeneity is equal to 1, the Toth model equation is reduced to the Langmuir isotherm [27]. On the other hand, if it deviates away from the unity state, then the adsorption system is considered heterogeneous [101]. Considering the theory of the above model

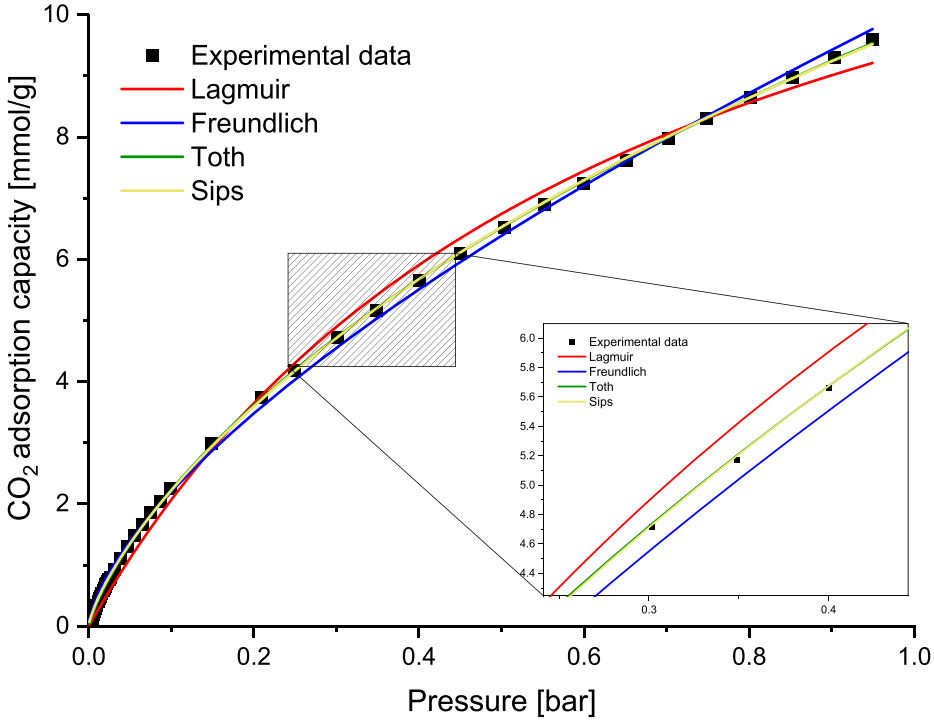

Fig. 12. CO_2 adsorption isotherm model curves for AC-800 at 0 °C. (A colour version of this figure can be viewed online.)

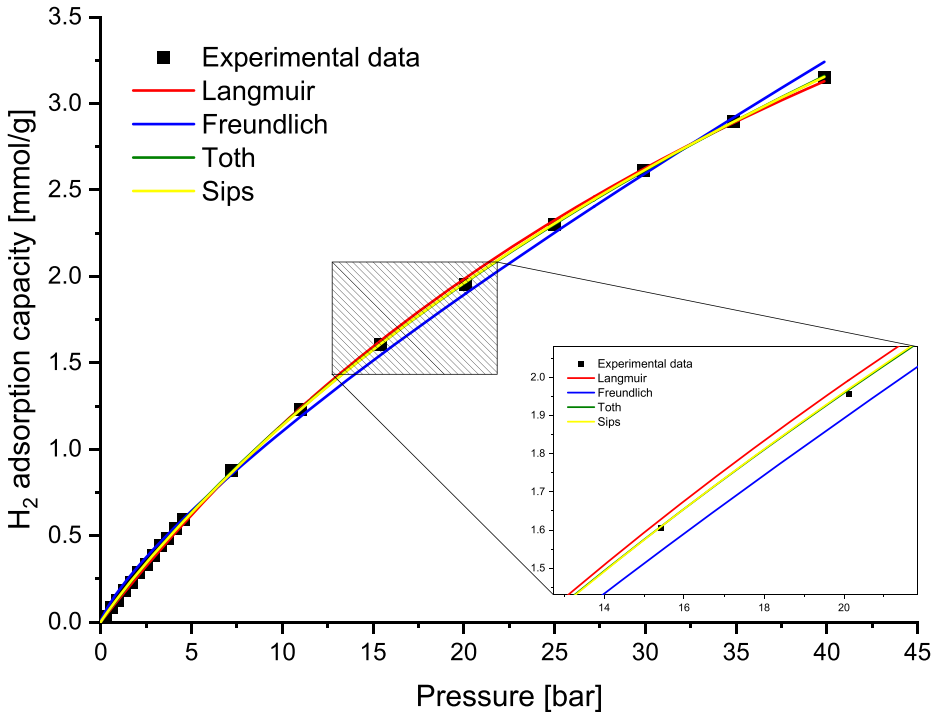

Fig. 13. H_2 adsorption isotherm model curves for AC-800 at 25 °C. (A colour version of this figure can be viewed online.)

and analyzing its, each AC sample at three CO_2 adsorption temperatures indicates that the surface of the adsorbent is heterogeneous. The values of n_T for the H_2 isotherm at 25 °C also indicate adsorption on an energetically heterogeneous surface.

3.8.3. *Sum of normalized errors method (SNE)*

To further study whether the sum of squares error (ERRSQ) is the optimal tool that best describes the interaction between the adsorbate and the surface of the AC for the best fitted model, other error functions have been employed (R^2, ARE, χ^2, HYBRID, MPSD, and EABS). The final error analysis based on the sum of normalized error (SNE) allowed for the verification of the previous conclusions with a more in-depth understanding of isotherm modeling in the sense of choosing the appropriate error evaluation function to minimize the error distribution between the experimental equilibrium data and theoretical isotherms. The error functions with connected the lowest SNE values are presented in Table 6 and Table 7.

In terms of minimizing the error distribution between the Toth isotherm model and the experimental equilibrium data of CO_2, the findings demonstrate that the determination coefficient (R^2) is superior to all the others investigated. The R^2 showed the lowest SNE value at each adsorption temperature than other error functions. Meanwhile, the results of the error analysis of the fitting to the H_2 experimental data indicated that the HYBRID and χ^2 error functions produced an optimum parameter set for the Toth isotherm due to their small SNE values. For the isothermal modeling of CO_2 and H_2, MPSD had the worst goodness of fit of the Toth model, due to the very large SNE (5.193–6.993).

Finally, it was found that, the use of ERRSQ error is not sufficient and the outputs of R^2, HYBRID and χ^2 may be used to forecast the optimal isotherm based on the three parameter Toth isotherm model. The

Table 6
The lowest sum of normalized error (SNE) values and the corresponding error function for Toth isotherm model.

Samples	Temperature 0 °C						
	R^2	ERRSQ	ARE	χ^2	HYBRID	MPSD	EABS
AC-500	**2.394**	3.287	2.840	2.799	2.799	6.409	3.292
AC-600	**2.558**	3.565	2.901	2.776	2.776	6.463	3.354
AC-700	**1.033**	1.054	6.493	1.090	1.090	6.313	1.046
AC-800	**1.037**	1.052	6.481	1.090	1.090	6.312	1.046
AC-900	**1.149**	1.198	1.997	1.608	1.608	6.536	1.218
Temperature 25 °C							
AC-500	**1.304**	1.432	2.583	1.930	1.930	6.992	1.408
AC-600	**1.305**	1.432	2.575	1.930	2.076	6.992	1.429
AC-700	**1.314**	1.421	2.567	1.966	1.965	6.993	1.403
AC-800	**1.319**	1.420	2.665	1.918	1.916	6.992	1.478
AC-900	**1.303**	1.434	1.510	1.930	1.930	6.992	1.415
Temperature 40 °C							
AC-500	**1.412**	1.575	2.280	1.891	1.891	6.993	1.549
AC-600	**1.412**	1.582	2.449	1.898	1.898	7.000	1.531
AC-700	**1.415**	1.581	2.560	1.891	1.891	6.993	1.580
AC-800	**1.564**	1.726	3.161	2.188	2.188	8.451	1.846
AC-900	**1.411**	1.574	1.545	1.891	1.891	6.993	1.681

Table 7
The lowest sum of normalized error (SNE) values and the corresponding error function for Toth isotherm model.

Samples	Temperature 25 °C						
	R^2	ERRSQ	ARE	χ^2	HYBRID	MPSD	EABS
AC-500	2.557	2.558	2.420	2.461	**2.461**	5.193	2.660
AC-600	2.449	2.450	2.186	2.222	**2.222**	6.775	2.366
AC-700	3.237	3.239	3.268	2.913	**2.913**	6.601	3.125
AC-800	2.604	2.605	2.550	**2.462**	2.462	6.258	2.544
AC-900	3.817	3.818	3.760	3.639	**3.639**	**6.742**	3.827

Table 8
CO_2/N_2 selectivity based on distinct numerical methods for all prepared samples.

Samples	S[a]		S_{IAST}[b]	
	25 °C	40 °C	25 °C	40 °C
AC-500	11.9	11.7	31.5	31.2
AC-600	15.4	16.5	56.6	31.1
AC-700	22.6	24.4	86	56.4
AC-800	43.6	48.7	163	102.3
AC-900	7.9	6.9	22.9	19.3

[a] CO_2 and N_2 binary mixture at temperatures (25 °C, and 40 °C) and 1 bar.
[b] CO_2/N_2 selectivity determined by IAST method at temperatures (25 °C, and 40 °C) and 1 bar.

findings shows that the magnitude of the single error function is not a determining factor in selecting the optimal isotherm parameters and the SNE method gives much better accuracy.

3.9. Studies of the CO_2 over N_2 selectivity

To test the gas CO_2/N_2 selectivity of the as-prepared carbons, their N_2 and CO_2 adsorption isotherms were acquired at 25 °C and 40 °C at 1 bar (Table 8, Fig. S5). The IAST theory developed by Myers and Prausnitz [102] along with pure component isotherms were applied to determine CO_2/N_2 selectivity. In this work, IAST was used to predict selectivity of CO_2 over N_2 using single adsorption isotherms of these gasses for equimolar CO_2 and N_2 binary mixture (S) according to the following equation:

$$S = \frac{qCO_2/qN_2}{pCO_2/pN_2} \quad (6)$$

where:

q represents the mole fractions of the components in adsorbed phase while p is used for bulk phase.

Typical flue gas composition in vol% is: 67–72% nitrogen, 8–10% carbon dioxide, 18–20% water steam, 2–3% oxygen for natural gas-fired power plants and 72–77% nitrogen, 12–14% carbon dioxide, 8–10% water steam, 3–5% oxygen for coal-fired boilers [72].

Selectivity for flue gas composition 15% CO_2 and 85% N_2 (S_{IAST}) was calculated also on the basis of IAST method using the below equation [64]:

$$S_{IAST} = \frac{q_{CO2}@0.15\ \text{bar}}{q_{N2}@0.85\ \text{bar}}\ x\ \frac{0.85}{0.15} \quad (7)$$

where:

qi@jbar is the adsorption capacity [mmol/g] of CO2 and N2 at the partial pressure of 0.15 and 0.85 respectively.

Table 8 shows the selectivity of the obtained activated carbons. The highest selectivity value was observed in AC-800, attributed to the effect of the potassium hydroxide activator and the facile accessibility of ultramicropores to CO_2 (diameter = 0.33 nm) but not to N_2 adsorption (0.36 nm) [103]. Moreover, a larger quadrupole moment of 4.30×10^{-26} esu*cm^2 of CO_2 compared to N_2 (1.52×10^{-26} esu*cm^2) [104] lead to stronger interactions between CO_2 molecules and adsorbent surfaces, resulting in highly selective CO_2 adsorption and separation. The value of the selectivity coefficient reaching the value of 43.6 and 48.7 for a pressure of 1 bar, respectively at 0 °C and 25 °C. It is worth noting that the obtained SIAST value is one of the highest so far described in the literature. A similar tendency in the CO_2/N_2 selectivity ratio was noted by Serafin et al. [64].

3.10. Stability tests of CO_2 and H_2 capture

One of the important criteria of a good activated carbon as an adsorbent is its regenerative capacity, which determines the life of the adsorbent, its reuse and the overall cost of capture. To determine the possibility of easy regeneration and reuse of the material, the reversibility of CO_2 adsorption was tested in 1,5,10,15,20 cycles and H_2 in 1,5,10 cycles for the best material AC-800 (Fig. 14). On this basis, it is possible to assess the possibility of regenerating activated carbons, and secondly, to verify the fact that CO_2 and H_2 do not bind to the sorbent material by chemisorption. Moreover, it enables parameters to be established that can serve as a benchmark when attempting to regenerate under real industrial scale conditions. Both in the case of CO_2 adsorption and H_2 adsorption, no changes were found after many cycles. The highest standard deviation for CO_2 cycles at 25 °C was 0.06 and at 40 °C was 0.08. For H_2 cycles, the standard deviation was 0.05. This is confirmed by the fact that it can be easily regenerated under mild conditions and the material retained its capacity. The obtained AC-800 activated carbon meets the criterion of a good sorbent in terms of its ability to regenerate.

4. Conclusions

This article discussed the key role of surface morphology as well as surface functionality on the substantial CO_2 and H_2 uptake capacity of walnut shells activated carbons. It can be concluded that the CO_2 and H_2 adsorption capacity on biomass-derived AC depends mainly on surface microporosity. The activation temperature had an effect on the pore structure, surface area and the adsorption properties of the activated carbons. As the activation temperature increased till 800 °C, the CO_2 and H_2 value increased first then decreased, and the yield declined continuously. The activation temperature 800 °C was the best stages of the activation process. The highest specific surface area, the total pore volume and micropore volume from CO_2 were 1868 m^2/g, 1.06 cm^3/g and 0.55 cm^3/g. CO_2 adsorption for the best activated carbon was 9.54, 5.17, 4.33 mmol/g for OC, 25 °C and 40 °C, respectively. However, in the case of high-pressure hydrogen adsorption, the highest value was 3.15 mmol/g. In addition, it is worth paying attention to the high selectivity of activated carbon at 25 °C = 163 and 40 °C = 102.3, as well as high stability after many adsorption cycles - both in the case of CO_2

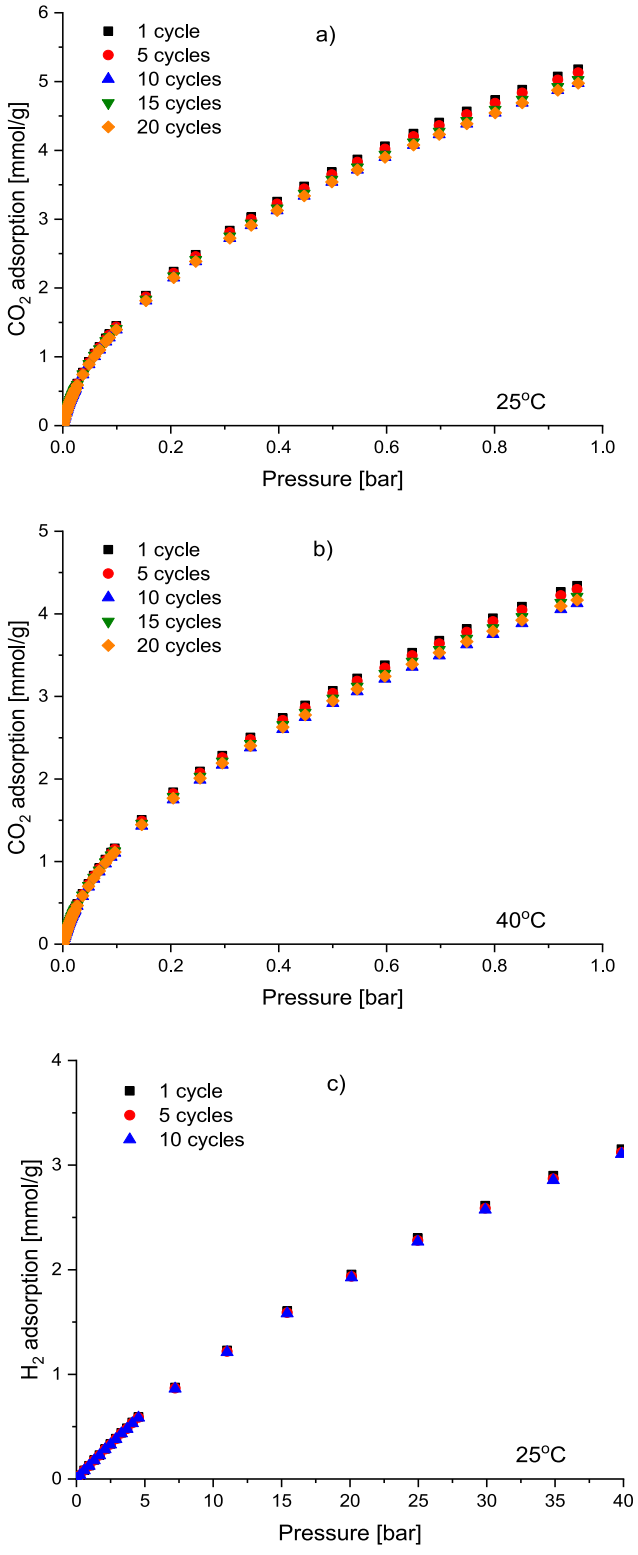

Fig. 14. Multi-cycle CO_2 adsorption isotherms for AC-800 at 25 °C and 40 °C in 1st, 10th, 20th adsorption isotherm and H_2 adsorption isotherms at 25 °C in 1st, 5th, 10th cycles for AC-800. (A colour version of this figure can be viewed online.)

and H_2.

CRediT authorship contribution statement

Jarosław Serafin: Conceptualization, Methodology, Validation, Formal analysis, Investigation, Data curation, Writing – original draft, Writing – review & editing, Project administration, Supervision. **Bartosz Dziejarski:** Software, Formal analysis, Investigation, Data curation, Writing – original draft, Writing – review & editing. **Orlando F. Cruz Junior:** Formal analysis, Writing – original draft, Editing. **Joanna Sreńscek-Nazzal:** Methodology, Validation, Formal analysis, Investigation, Writing – original draft, Editing.

Declaration of competing interest

The authors declare that they have no known competing financial interests or personal relationships that could have appeared to influence the work reported in this paper.

Acknowledgements

Jarosław Serafin is grateful to Spanish Ministry of Research and Innovation project no: PID2020-116031RBI00/AEI/10.13039/501100011033/FEDER.

Appendix A. Supplementary data

Supplementary data to this article can be found online at https://doi.org/10.1016/j.carbon.2022.09.013.

References

[1] E. Purba, Taharuddin, CO(2) reduction and production of algal oil using microalgae nannochloropsis oculata and tetraselmis chuii, Chem. Eng. Trans. (2010) 397–402, https://doi.org/10.3303/CET1021067.
[2] J. Serafin, M. Ouzzine, J. Sreńscek-Nazzal, J. Llorca, Photocatalytic hydrogen production from alcohol aqueous solutions over TiO2-activated carbon composites decorated with Au and Pt, J. Photochem. Photobiol. Chem. 425 (2022), 113726, https://doi.org/10.1016/j.jphotochem.2021.113726.
[3] B.D. Solomon, A. Banerjee, A global survey of hydrogen energy research, development and policy, Energy Pol. 34 (2006) 781–792, https://doi.org/10.1016/J.ENPOL.2004.08.007.
[4] C. Dhoke, A. Zaabout, S. Cloete, S. Amini, Review on reactor configurations for adsorption-based CO2 capture, Ind. Eng. Chem. Res. 60 (2021) 3779–3798, https://doi.org/10.1021/acs.iecr.0c04547.
[5] P. Ammendola, F. Raganati, R. Chirone, CO2 adsorption on a fine activated carbon in a sound assisted fluidized bed: thermodynamics and kinetics, Chem. Eng. J. 322 (2017) 302–313, https://doi.org/10.1016/J.CEJ.2017.04.037.
[6] S. Sahoo Gautam, Experimental investigation on different activated carbons as adsorbents for CO2 capture, Therm. Sci. Eng. Prog. 33 (2022), 101339, https://doi.org/10.1016/J.TSEP.2022.101339.
[7] A. Okhovat, A. Ahmadpour, F. Ahmadpour, Z. Khaki Yadegar, Pore size distribution analysis of coal-based activated carbons: investigating the effects of activating agent and chemical ratio, ISRN Chem. Eng. 2012 (2012) 1–10, https://doi.org/10.5402/2012/352574.
[8] C. Srinivasakannan, M. Zailani Abu Bakar, Production of activated carbon from rubber wood sawdust, Biomass Bioenergy 27 (2004) 89–96, https://doi.org/10.1016/j.biombioe.2003.11.002.
[9] M. Kwiatkowski, E. Broniek, An analysis of the porous structure of activated carbons obtained from hazelnut shells by various physical and chemical methods of activation, Colloids Surf. A Physicochem. Eng. Asp. 529 (2017) 443–453, https://doi.org/10.1016/j.colsurfa.2017.06.028.
[10] Y. Song, T. Liu, F. Qian, C. Zhu, B. Yao, E. Duoss, C. Spadaccini, M. Worsley, Y. Li, Three-dimensional carbon architectures for electrochemical capacitors, J. Colloid Interface Sci. 509 (2018) 529–545, https://doi.org/10.1016/j.jcis.2017.07.081.
[11] M. Al Bahri, L. Calvo, M.A. Gilarranz, J.J. Rodriguez, Diuron multilayer adsorption on activated carbon from CO 2 activation of grape seeds, Chem. Eng. Commun. 203 (2016) 103–113, https://doi.org/10.1080/00986445.2014.934447.
[12] A.-N.A. El-Hendawy, A.J. Alexander, R.J. Andrews, G. Forrest, Effects of activation schemes on porous, surface and thermal properties of activated

carbons prepared from cotton stalks, J. Anal. Appl. Pyrolysis 82 (2008) 272–278, https://doi.org/10.1016/j.jaap.2008.04.006.
[13] T. Tay, S. Ucar, S. Karagöz, Preparation and characterization of activated carbon from waste biomass, J. Hazard Mater. 165 (2009) 481–485, https://doi.org/10.1016/j.jhazmat.2008.10.011.
[14] G. Li, F. Tian, Y. Zhang, J. Ding, Y. Fu, Y. Wang, G. Zhang, Bamboo/lignite-based activated carbons produced by steam activation with and without ammonia for SO2 adsorption, Carbon N. Y. 85 (2015) 448, https://doi.org/10.1016/j.carbon.2014.12.083.
[15] A. Wróblewska, J. Serafin, A. Gawarecka, P. Miądlicki, K. Urbaś, Z.C. Koren, J. Llorca, B. Michalkiewicz, Carbonaceous catalysts from orange pulp for limonene oxidation, Carbon Lett. 30 (2020) 189–198, https://doi.org/10.1007/s42823-019-00084-2.
[16] N. Abuelnoor, A. AlHajaj, M. Khaleel, L.F. Vega, M.R.M. Abu-Zahra, Activated carbons from biomass-based sources for CO2 capture applications, Chemosphere 282 (2021), 131111, https://doi.org/10.1016/j.chemosphere.2021.131111.
[17] W. Koo-amornpattana, W. Jonglertjunya, P. Phadungbut, S. Ratchahat, N. Kunthakudee, B. Chalermsinsuwan, M. Hunsom, Valorization of spent disposable wooden chopstick as the CO2 adsorbent for a CO2/H2 mixed gas purification, Sci. Rep. 12 (2022) 6250, https://doi.org/10.1038/s41598-022-10197-w.
[18] D. Sibera, J. Srenscek-Nazzal, W.A. Morawski, B. Michalkiewicz, J. Serafin, R. J. Wróbel, U. Narkiewicz, Microporous carbon spheres modified with EDA used as carbon dioxide sorbents, Adv. Mater. Lett. 9 (2018) 432–435, https://doi.org/10.5185/amlett.2018.1872.
[19] C. Zhang, Z. Geng, M. Cai, J. Zhang, X. Liu, H. Xin, J. Ma, Microstructure regulation of super activated carbon from biomass source corncob with enhanced hydrogen uptake, Int. J. Hydrogen Energy 38 (2013) 9243–9250, https://doi.org/10.1016/j.ijhydene.2013.04.163.
[20] M.M. de Castro, M. Martínez-Escandell, M. Molina-Sabio, F. Rodríguez-Reinoso, Hydrogen adsorption on KOH activated carbons from mesophase pitch containing Si, B, Ti or Fe, Carbon N. Y. 48 (2010) 636–644, https://doi.org/10.1016/j.carbon.2009.10.005.
[21] I. Wróbel-Iwaniec, N. Díez, G. Gryglewicz, Chitosan-based highly activated carbons for hydrogen storage, Int. J. Hydrogen Energy 40 (2015) 5788–5796, https://doi.org/10.1016/j.ijhydene.2015.03.034.
[22] M. Sevilla, A.B. Fuertes, R. Mokaya, High density hydrogen storage in superactivated carbons from hydrothermally carbonized renewable organic materials, Energy Environ. Sci. 4 (2011) 1400, https://doi.org/10.1039/c0ee00347f.
[23] C. Zhang, W. Song, Q. Ma, L. Xie, X. Zhang, H. Guo, Enhancement of CO 2 capture on biomass-based carbon from black locust by KOH activation and ammonia modification, Energy Fuel. 30 (2016) 4181–4190, https://doi.org/10.1021/acs.energyfuels.5b02764.
[24] J. Serafin, Utilization of spent dregs for the production of activated carbon for CO 2 adsorption, Pol. J. Chem. Technol. 19 (2017) 44–50, https://doi.org/10.1515/pjct-2017-0026.
[25] D. Li, Y. Tian, L. Li, J. Li, H. Zhang, Production of highly microporous carbons with large CO2 uptakes at atmospheric pressure by KOH activation of peanut shell char, J. Porous Mater. 22 (2015) 1581–1588, https://doi.org/10.1007/s10934-015-0041-7.
[26] M.I. El-Khaiary, Least-squares regression of adsorption equilibrium data: comparing the options, J. Hazard Mater. 158 (2008) 73–87, https://doi.org/10.1016/j.jhazmat.2008.01.052.
[27] N. Ayawei, A.N. Ebelegi, D. Wankasi, Modelling and interpretation of adsorption isotherms, J. Chem. 2017 (2017) 1–11, https://doi.org/10.1155/2017/3039817.
[28] J. Tóth, State Equation of the Solid-Gas Interface Layers, 1971.
[29] R. Sips, On the structure of a catalyst surface, J. Chem. Phys. 16 (1948) 490–495, https://doi.org/10.1063/1.1746922.
[30] M. Thommes, K. Kaneko, A.V. Neimark, J.P. Olivier, F. Rodriguez-reinoso, J. Rouquerol, K.S.W.W. Sing, Physisorption of gases , with special reference to the evaluation of surface area and pore size distribution (IUPAC Technical Report), Pure Appl. Chem. 87 (2015) 1051–1069, https://doi.org/10.1515/pac-2014-1117.
[31] R. Melouki, A. Ouadah, P.L. Llewellyn, The CO2 adsorption behavior study on activated carbon synthesized from olive waste, J. CO2 Util. 42 (2020), 101292, https://doi.org/10.1016/j.jcou.2020.101292.
[32] M. Lillo-Ródenas, D. Cazorla-Amorós, A. Linares-Solano, Understanding chemical reactions between carbons and NaOH and KOH, Carbon N. Y. 41 (2003) 267–275, https://doi.org/10.1016/S0008-6223(02)00279-8.
[33] K.Y. Foo, B.H. Hameed, Insights into the modeling of adsorption isotherm systems, Chem. Eng. J. 156 (2010) 2–10, https://doi.org/10.1016/j.cej.2009.09.013.
[34] K.V. Kumar, K. Porkodi, F. Rocha, Isotherms and thermodynamics by linear and non-linear regression analysis for the sorption of methylene blue onto activated carbon: comparison of various error functions, J. Hazard Mater. 151 (2008) 794–804, https://doi.org/10.1016/j.jhazmat.2007.06.056.
[35] J.C. Ng, W. Cheung, G. McKay, Equilibrium studies of the sorption of Cu(II) ions onto chitosan, J. Colloid Interface Sci. 255 (2002) 64–74, https://doi.org/10.1006/jcis.2002.8664.
[36] G. Huang, Y. Liu, X. Wu, J. Cai, Activated carbons prepared by the KOH activation of a hydrochar from garlic peel and their CO2 adsorption performance, N. Carbon Mater. 34 (2019) 247–257, https://doi.org/10.1016/S1872-5805(19)60014-4.
[37] X. Lan, X. Jiang, Y. Song, X. Jing, X. Xing, The effect of activation temperature on structure and properties of blue coke-based activated carbon by CO2 activation, Green Process. Synth. 8 (2019) 837–845, https://doi.org/10.1515/gps-2019-0054.
[38] Y. Diao, W. Walawender, L. Fan, Activated carbons prepared from phosphoric acid activation of grain sorghum, Bioresour. Technol. 81 (2002) 45–52, https://doi.org/10.1016/S0960-8524(01)00100-6.
[39] M. Molina-Sabio, F. RodRíguez-Reinoso, F. Caturla, M.J. Sellés, Porosity in granular carbons activated with phosphoric acid, Carbon N. Y. 33 (1995) 1105–1113, https://doi.org/10.1016/0008-6223(95)00059-M.
[40] D. Kouotou, H.N. Manga, A. Baçaoui, A. Yaacoubi, J.K. Mbadcam, Optimization of Activated Carbons Prepared by H_3PO_4 and Steam Activation of Oil Palm Shells, J. Chem. 2013 (2013) 1–10, https://doi.org/10.1155/2013/654343.
[41] M.K.B. Gratuito, T. Panyathanmaporn, R.-A. Chumnanklang, N. Sirinuntawittaya, A. Dutta, Production of activated carbon from coconut shell: optimization using response surface methodology, Bioresour. Technol. 99 (2008) 4887–4895, https://doi.org/10.1016/j.biortech.2007.09.042.
[42] D. Mallesh, J. Anbarasan, P. Mahesh Kumar, K. Upendar, P. Chandrashekar, B.V. S.K. Rao, N. Lingaiah, Synthesis, characterization of carbon adsorbents derived from waste biomass and its application to CO2 capture, Appl. Surf. Sci. 530 (2020), 147226, https://doi.org/10.1016/j.apsusc.2020.147226.
[43] R. Zhang, Q. Hou, Y. Wang, W. Zhu, J. Fan, M. Zheng, Q. Dong, A biomass-based hierarchical carbon via MOFs-assisted synthesis for high-rate lithium-ion storage, Electrochem. Commun. 139 (2022), 107310, https://doi.org/10.1016/j.elecom.2022.107310.
[44] R. Zhang, J. Qiao, X. Zhang, Y. Yang, S. Zheng, B. Li, W. Liu, J. Liu, Z. Zeng, Biomass-derived porous carbon for microwave absorption, Mater. Chem. Phys. 289 (2022), 126437, https://doi.org/10.1016/j.matchemphys.2022.126437.
[45] Z. Tian, Y. Qiu, J. Zhou, X. Zhao, J. Cai, The direct carbonization of algae biomass to hierarchical porous carbons and CO2 adsorption properties, Mater. Lett. 180 (2016) 162–165, https://doi.org/10.1016/j.matlet.2016.05.169.
[46] M. Keiluweit, P.S. Nico, M.G. Johnson, M. Kleber, Dynamic molecular structure of plant biomass-derived black carbon (biochar), Environ. Sci. Technol. 44 (2010) 1247–1253, https://doi.org/10.1021/es9031419.
[47] Q. Pu, J. Zou, J. Wang, S. Lu, P. Ning, L. Huang, Q. Wang, Systematic study of dynamic CO2 adsorption on activated carbons derived from different biomass, J. Alloys Compd. 887 (2021), 161406, https://doi.org/10.1016/j.jallcom.2021.161406.
[48] C.J. Durán-Valle, M. Gómez-Corzo, J. Pastor-Villegas, V. Gómez-Serrano, Study of cherry stones as raw material in preparation of carbonaceous adsorbents, J. Anal. Appl. Pyrolysis 73 (2005) 59–67, https://doi.org/10.1016/j.jaap.2004.10.004.
[49] C. Ma, J. Min, J. Gong, X. Liu, X. Mu, X. Chen, T. Tang, Transforming polystyrene waste into 3D hierarchically porous carbon for high-performance supercapacitors, Chemosphere 253 (2020), 126755, https://doi.org/10.1016/j.chemosphere.2020.126755.
[50] X. Ma, S. Li, V. Hessel, L. Lin, S. Meskers, F. Gallucci, Synthesis of luminescent carbon quantum dots by microplasma process, Chem. Eng. Process. - Process Intensif. 140 (2019) 29–35, https://doi.org/10.1016/j.cep.2019.04.017.
[51] W. Bae, J. Kim, J. Chung, Production of granular activated carbon from food-processing wastes (walnut shells and jujube seeds) and its adsorptive properties, J. Air Waste Manage. Assoc. 64 (2014) 879–886, https://doi.org/10.1080/10962247.2014.897272.
[52] S. cheng, L. Zhang, H. Xia, J. Peng, S. Zhang, S. Wang, Preparation of high specific surface area activated carbon from walnut shells by microwave-induced KOH activation, J. Porous Mater. 22 (2015) 1527–1537, https://doi.org/10.1007/s10934-015-0035-5.
[53] D. Lan, M. Chen, Y. Liu, Q. Liang, W. Tu, Y. Chen, J. Liang, F. Qiu, Preparation and characterization of high value-added activated carbon derived from biowaste walnut shell by KOH activation for supercapacitor electrode, J. Mater. Sci. Mater. Electron. 31 (2020) 18541–18553, https://doi.org/10.1007/s10854-020-04398-0.
[54] A. Aygün, S. Yenisoy-Karakaş, I. Duman, Production of granular activated carbon from fruit stones and nutshells and evaluation of their physical, chemical and adsorption properties, Microporous Mesoporous Mater. 66 (2003) 189–195, https://doi.org/10.1016/j.micromeso.2003.08.028.
[55] E. Yagmur, M. Ozmak, Z. Aktas, A novel method for production of activated carbon from waste tea by chemical activation with microwave energy, Fuel 87 (2008) 3278–3285, https://doi.org/10.1016/j.fuel.2008.05.005.
[56] P.T. Williams, A.R. Reed, High grade activated carbon matting derived from the chemical activation and pyrolysis of natural fibre textile waste, J. Anal. Appl. Pyrolysis 71 (2004) 971–986, https://doi.org/10.1016/j.jaap.2003.12.007.
[57] V. Fierro, V. Torné-Fernández, A. Celzard, Kraft lignin as a precursor for microporous activated carbons prepared by impregnation with ortho-phosphoric acid: synthesis and textural characterisation, Microporous Mesoporous Mater. 92 (2006) 243–250, https://doi.org/10.1016/j.micromeso.2006.01.013.
[58] W. Xing, C. Liu, Z. Zhou, L. Zhang, J. Zhou, S. Zhuo, Z. Yan, H. Gao, G. Wang, S. Z. Qiao, Superior CO2 uptake of N-doped activated carbon through hydrogen-bonding interaction, Energy Environ. Sci. 5 (2012) 7323, https://doi.org/10.1039/c2ee21653a.
[59] M. Idrees, V. Rangari, S. Jeelani, Sustainable packaging waste-derived activated carbon for carbon dioxide capture, J. CO2 Util. 26 (2018) 380–387, https://doi.org/10.1016/J.JCOU.2018.05.016.
[60] M.K. Al Mesfer, Synthesis and characterization of high-performance activated carbon from walnut shell biomass for CO2 capture, Environ. Sci. Pollut. Res. 27 (2020) 15020–15028, https://doi.org/10.1007/s11356-020-07934-x.
[61] A. Alabadi, S. Razzaque, Y. Yang, S. Chen, B. Tan, Highly porous activated carbon materials from carbonized biomass with high CO2 capturing capacity, Chem. Eng. J. 281 (2015) 606–612, https://doi.org/10.1016/j.cej.2015.06.032.

[62] M. Grundy, Z. Ye, Cross-linked polymers of diethynylbenzene and phenylacetylene as new polymer precursors for high-yield synthesis of high-performance nanoporous activated carbons for supercapacitors, hydrogen storage, and CO 2 capture, J. Mater. Chem. A. 2 (2014) 20316–20330, https://doi.org/10.1039/C4TA04038D.
[63] L.F.A.S. Zafanelli, A. Henrique, H. Steldinger, J.L. Diaz de Tuesta, J. Gläsel, A. E. Rodrigues, H.T. Gomes, B.J.M. Etzold, J.A.C. Silva, 3D-printed activated carbon for post-combustion CO2 capture, Microporous Mesoporous Mater. 335 (2022), 111818, https://doi.org/10.1016/J.MICROMESO.2022.111818.
[64] J. Serafin, J. Sreńscek-Nazzal, A. Kamińska, O. Paszkiewicz, B. Michalkiewicz, Management of surgical mask waste to activated carbons for CO2 capture, J. CO2 Util. 59 (2022), 101970, https://doi.org/10.1016/j.jcou.2022.101970.
[65] S. Deng, H. Wei, T. Chen, B. Wang, J. Huang, G. Yu, Superior CO2 adsorption on pine nut shell-derived activated carbons and the effective micropores at different temperatures, Chem. Eng. J. 253 (2014) 46–54, https://doi.org/10.1016/j.cej.2014.04.115.
[66] D. Li, T. Ma, R. Zhang, Y. Tian, Y. Qiao, Preparation of porous carbons with high low-pressure CO2 uptake by KOH activation of rice husk char, Fuel 139 (2015) 68–70, https://doi.org/10.1016/j.fuel.2014.08.027.
[67] J. Choma, M. Marszewski, L. Osuchowski, J. Jagiello, A. Dziura, M. Jaroniec, Adsorption properties of activated carbons prepared from waste CDs and DVDs, ACS Sustain. Chem. Eng. 3 (2015) 733–742, https://doi.org/10.1021/acssuschemeng.5b00036.
[68] E. Gomez-Delgado, G. Nunell, A.L. Cukierman, P. Bonelli, Tailoring activated carbons from Pinus canariensis cones for post-combustion CO2 capture, Environ. Sci. Pollut. Res. 27 (2020) 13915–13929, https://doi.org/10.1007/s11356-020-07830-4.
[69] J. Chen, J. Yang, G. Hu, X. Hu, Z. Li, S. Shen, M. Radosz, M. Fan, Enhanced CO2 capture capacity of nitrogen-doped biomass-derived porous carbons, ACS Sustain. Chem. Eng. 4 (2016) 1439–1445, https://doi.org/10.1021/acssuschemeng.5b01425.
[70] O. Boujibar, A. Souikny, F. Ghamouss, O. Achak, M. Dahbi, T. Chafik, CO2 capture using N-containing nanoporous activated carbon obtained from argan fruit shells, J. Environ. Chem. Eng. 6 (2018) 1995–2002, https://doi.org/10.1016/J.JECE.2018.03.005.
[71] J. Zhou, D. Li, Y. Wang, Y. Tian, Z. Zhang, L. Wei, W. Feng, Effect of the feedstock type on the volumetric low-pressure CO 2 capture performance of activated carbons, Energy Fuel. 32 (2018) 12711–12720, https://doi.org/10.1021/acs.energyfuels.8b02827.
[72] J. Serafin, K. Kiełbasa, B. Michalkiewicz, The new tailored nanoporous carbons from the common polypody (Polypodium vulgare): the role of textural properties for enhanced CO2 adsorption, Chem. Eng. J. 429 (2022), 131751, https://doi.org/10.1016/j.cej.2021.131751.
[73] X.-L.L. Zhu, P.-Y.Y. Wang, C. Peng, J. Yang, X.-B. Bin Yan, Activated carbon produced from paulownia sawdust for high-performance CO2 sorbents, Chin. Chem. Lett. 25 (2014) 929–932, https://doi.org/10.1016/j.cclet.2014.03.039.
[74] A. Modak, A. Bhaumik, Porous carbon derived via KOH activation of a hypercrosslinked porous organic polymer for efficient CO2, CH4, H2 adsorptions and high CO2/N2 selectivity, J. Solid State Chem. 232 (2015) 157–162, https://doi.org/10.1016/j.jssc.2015.09.022.
[75] N.P. Wickramaratne, M. Jaroniec, Importance of small micropores in CO 2 capture by phenolic resin-based activated carbon spheres, J. Mater. Chem. A. 1 (2013) 112–116, https://doi.org/10.1039/C2TA00388K.
[76] K. Rouquerol, F, J. Rouquerol, Sing, Adsorption by Powders and Porous Solids: Principles, Methodology and Application, 1 st, Academic Press, 1999. www.elsevier.com/books/adsorption-by-powders-and-porous-solids/rouquerol/978-0-08-097035-6.
[77] G. Conte, A. Policicchio, O. De Luca, P. Rudolf, G. Desiderio, R.G. Agostino, Copper-doped activated carbon from amorphous cellulose for hydrogen, methane and carbon dioxide storage, Int. J. Hydrogen Energy 47 (2022) 18384–18395, https://doi.org/10.1016/J.IJHYDENE.2022.04.029.
[78] S. Mirzaei, A. Ahmadpour, A. Shahsavand, A. Nakhaei Pour, L. LotfiKatooli, A. Garmroodi Asil, B. Pouladi, A. Arami-Niya, Experimental and simulation study of the effect of surface functional groups decoration on CH4 and H2 storage capacity of microporous carbons, Appl. Surf. Sci. 533 (2020), 147487, https://doi.org/10.1016/J.APSUSC.2020.147487.
[79] Z. Bicil, M. Doğan, Characterization of activated carbons prepared from almond shells and their hydrogen storage properties, Energy Fuel. 35 (2021) 10227–10240, https://doi.org/10.1021/acs.energyfuels.1c00795.
[80] Y. Sun, P.A. Webley, Preparation of activated carbons from corncob with large specific surface area by a variety of chemical activators and their application in gas storage, Chem. Eng. J. 162 (2010) 883–892, https://doi.org/10.1016/J.CEJ.2010.06.031.
[81] N. Kaya, Z.Y. Uzun, Investigation of effectiveness of pine cone biochar activated with KOH for methyl orange adsorption and CO2 capture, Biomass Convers. Biorefinery. 11 (2021) 1067–1083, https://doi.org/10.1007/s13399-020-01063-8.
[82] M. Jung, J. Park, K. Lee, N.F. Attia, H. Oh, Effective synthesis route of renewable nanoporous carbon adsorbent for high energy gas storage and CO2/N2 selectivity, Renew. Energy 161 (2020) 30–42, https://doi.org/10.1016/j.renene.2020.06.125.
[83] N.F. Attia, M. Jung, J. Park, H. Jang, K. Lee, H. Oh, Flexible nanoporous activated carbon cloth for achieving high H2, CH4, and CO2 storage capacities and selective CO2/CH4 separation, Chem. Eng. J. 379 (2020), 122367, https://doi.org/10.1016/j.cej.2019.122367.
[84] T.S. Blankenship, N. Balahmar, R. Mokaya, Oxygen-rich microporous carbons with exceptional hydrogen storage capacity, Nat. Commun. 8 (2017), https://doi.org/10.1038/s41467-017-01633-x.
[85] R. Pedicini, S. Maisano, V. Chiodo, G. Conte, A. Policicchio, R.G. Agostino, Posidonia Oceanica and Wood chips activated carbon as interesting materials for hydrogen storage, Int. J. Hydrogen Energy 45 (2020) 14038–14047, https://doi.org/10.1016/J.IJHYDENE.2020.03.130.
[86] S. Schaefer, V. Fierro, M.T. Izquierdo, A. Celzard, Assessment of hydrogen storage in activated carbons produced from hydrothermally treated organic materials, Int. J. Hydrogen Energy 41 (2016) 12146–12156, https://doi.org/10.1016/J.IJHYDENE.2016.05.086.
[87] H.M. Lee, Y.J. Heo, K.H. An, S.C. Jung, D.C. Chung, S.J. Park, B.J. Kim, A study on optimal pore range for high pressure hydrogen storage behaviors by porous hard carbon materials prepared from a polymeric precursor, Int. J. Hydrogen Energy 43 (2018) 5894–5902, https://doi.org/10.1016/J.IJHYDENE.2017.09.085.
[88] N. Kostoglou, C. Koczwara, S. Stock, C. Tampaxis, G. Charalambopoulou, T. Steriotis, O. Paris, C. Rebholz, C. Mitterer, Nanoporous polymer-derived activated carbon for hydrogen adsorption and electrochemical energy storage, Chem. Eng. J. 427 (2022), 131730, https://doi.org/10.1016/J.CEJ.2021.131730.
[89] M.S. Balathanigaimani, M.B. Haider, D. Jha, R. Kumar, S.J. Lee, W.G. Shim, H. K. Shon, S.C. Kim, H. Moon, Nanostructured biomass based carbon materials from beer lees for hydrogen storage, J. Nanosci. Nanotechnol. 18 (2018) 2196–2199, https://doi.org/10.1166/jnn.2018.15001.
[90] L. Ma, J. Li, X. Ma, Preparation and adsorption of CO2 and H2 by activated carbon hollow fibers from rubber wood (Hevea brasiliensis), Bioresources 14 (2019) 9755–9765, https://doi.org/10.15376/biores.14.4.9755-9765.
[91] T. Ramesh, N. Rajalakshmi, K.S. Dhathathreyan, Synthesis and characterization of activated carbon from jute fibers for hydrogen storage, Renew. Energy Environ. Sustain. 2 (2017) 4, https://doi.org/10.1051/rees/2017001.
[92] A.I. Sultana, N. Saha, M.T. Reza, M. Toufiq Reza, Synopsis of factors affecting hydrogen storage in biomass-derived activated carbons, Sustainability 13 (2021) 1947, https://doi.org/10.3390/su13041947.
[93] O. Czakkel, B. Nagy, G. Dobos, P. Fouquet, E. Bahn, K. László, Static and dynamic studies of hydrogen adsorption on nanoporous carbon gels, Int. J. Hydrogen Energy 44 (2019) 18169–18178, https://doi.org/10.1016/j.ijhydene.2019.05.131.
[94] N. Bader, R. Zacharia, O. Abdelmottaleb, D. Cossement, How the activation process modifies the hydrogen storage behavior of biomass-derived activated carbons, J. Porous Mater. 25 (2018) 221–234, https://doi.org/10.1007/s10934-017-0436-8.
[95] G. Yushin, R. Dash, J. Jagiello, J.E. Fischer, Y. Gogotsi, Carbide-derived carbons: effect of pore size on hydrogen uptake and heat of adsorption, Adv. Funct. Mater. 16 (2006) 2288–2293, https://doi.org/10.1002/adfm.200500830.
[96] X. Zhou, H. Yi, X. Tang, H. Deng, H. Liu, Thermodynamics for the adsorption of SO2, NO and CO2 from flue gas on activated carbon fiber, Chem. Eng. J. 200–202 (2012) 399–404, https://doi.org/10.1016/j.cej.2012.06.013.
[97] J.M. Simmons, H. Wu, W. Zhou, T. Yildirim, Carbon capture in metal–organic frameworks—a comparative study, Energy Environ. Sci. 4 (2011) 2177, https://doi.org/10.1039/c0ee00700e.
[98] K.S.W. Sing, D.H. Everett, R.A.W. Haul, L. Moscou, R.A. Pierotti, J. Rouquerol, T. Siemieniewska, Reporting physisorption data for gas/solid systems with special reference to the determination of surface area and porosity (Recommendations 1984), Pure Appl. Chem. 57 (1985) 603–619, https://doi.org/10.1351/pac198557040603.
[99] M.A. Al-Ghouti, D.A. Da'ana, Guidelines for the use and interpretation of adsorption isotherm models: a review, J. Hazard Mater. 393 (2020), 122383, https://doi.org/10.1016/j.jhazmat.2020.122383.
[100] F.-C. Wu, R.-L. Tseng, Liquid–solid phase countercurrent multi-stage adsorption process for using the Langmuir equation, J. Hazard Mater. 155 (2008) 449–458, https://doi.org/10.1016/j.jhazmat.2007.11.086.
[101] M.S. Podder, C.B. Majumder, Studies on the removal of As(III) and As(V) through their adsorption onto granular activated carbon/MnFe2O4 composite: isotherm studies and error analysis, Compos. Interfac. 23 (2016) 327–372, https://doi.org/10.1080/09276440.2016.1137715.
[102] A.L. Myers, J.M. Prausnitz, Thermodynamics of mixed-gas adsorption, AIChE J. 11 (1965) 121–127, https://doi.org/10.1002/aic.690110125.
[103] J. Yang, Q. Zhao, H. Xu, L. Li, J. Dong, J. Li, Adsorption of CO 2 , CH 4 , and N 2 on gas diameter grade ion-exchange small pore zeolites, J. Chem. Eng. Data 57 (2012) 3701–3709, https://doi.org/10.1021/je300940m.
[104] G. Nazir, A. Rehman, S.-J.J. Park, Role of heteroatoms (nitrogen and sulfur)-dual doped corn-starch based porous carbons for selective CO2 adsorption and separation, J. CO2 Util. 51 (2021), 101641, https://doi.org/10.1016/j.jcou.2021.101641.